

## 6

# Dynamics of Wall-Bounded Turbulence

Javier Jiménez and Genta Kawahara

### 6.1 Introduction

This chapter deals with the dynamics of wall-bounded turbulent flows, with a decided emphasis on the results of numerical simulations. As we will see, part of the reason for that emphasis is that much of the recent work on dynamics has been computational, but also that the companion chapter by Marusic and Adrian (2012) in this volume reviews the results of experiments over the same period.

The first direct numerical simulations (DNS) of wall-bounded turbulence (Kim et al., 1987) began to appear soon after computers became powerful enough to allow the simulation of turbulence in general (Siggia, 1981; Rogallo, 1981). Large-eddy simulations (LES) of wall-bounded flows had been published before (Deardorff, 1970; Moin and Kim, 1982) but, after DNS became current, they were de-emphasized as means of clarifying the flow physics, in part because doubts emerged about the effect of the poorly resolved near-wall region on the rest of the flow. Some of the work summarized below has eased those misgivings, and there are probably few reasons to distrust the information provided by LES on the largest flow structures, but any review of the physical results of numerics in the recent past necessarily has to deal mostly with DNS. Only atmospheric scientists, for whom the prospect of direct simulation remains remote, have continued to use LES to study the mechanics of the atmospheric surface layer (see, for example, Deardorff, 1973; Siebesma et al., 2003). A summary of the early years of numerical turbulence research can be found in Rogallo and Moin (1984) and Moin and Mahesh (1998). Here, we review the advances that have taken place in its application to wall-bounded flows since the first of those two papers, and, in particular, what we have learned during that time about

the physics of the flow. The interactions with experimental results will be discussed where appropriate.

First of all, it is important to emphasize that numerical simulations and experiments are different, although related, approximations to reality, and that they should not be expected to agree exactly with each other. For example, computing a channel in a doubly periodic domain is an approximation, in the same way as an experimental channel with a finite aspect ratio. In both cases, the parameters have to be chosen so that the resulting system approaches ‘closely enough’ the ideal channel of real interest, which is infinitely long and wide. Simulations only need to reproduce experiments, and vice versa, in the sense that they are both intended to approximate the same real object, and neither of the two is automatically to be preferred to the other.

Luckily, the strengths and weaknesses of the two techniques tend to be complementary. Simulations give precise answers to precisely posed and controlled problems, with precisely known initial and boundary conditions. No simulation can be run without fully stipulating all those factors, and the only limitation to our knowledge in that respect is how many data we choose to store. The situation is typically different in experiments, for which there are often unknown factors that are difficult to document, such as inflow conditions and wind tunnel imperfections. Those imperfections are different from the ones in numerics, but they are in no sense more ‘natural’. For example, it is tempting to consider that the random perturbations in the free stream of a wind tunnel are a ‘more natural’ trigger for transition than the deterministic perturbations typically introduced in simulations, but there is nothing random about the natural world, and the perturbations present in different experiments are as different from each other, and as different from the ones presumably present in our intended applications, as any deterministic perturbation imposed in a simulation. In most cases, randomness is not a virtue, but a measure of our ignorance.

Another difference that is often mentioned is that experiments are imperfect measurements of a ‘true’ system, while simulations are perfect measurements of something that is at best only an approximation. Both things are true, but only in the weak sense that it is not completely clear whether the Navier–Stokes equations represent fluid flow, or whether they have continuous unique solutions. The first concern is probably not worse than worrying about whether the air in a wind tunnel is a perfect gas, but the second is slightly more substantive. Numerical methods typically assume some continuity in the solutions that they represent, in which case their error bounds are extremely well understood and kept under tight control in most simu-

lations. The error associated with the numerical approximation is usually negligible compared with the statistical uncertainty. On the other hand, most simulation codes are designed to be ‘robust’, and to behave gracefully when an unexpected discontinuity is found. For that reason, they would probably miss a hypothetical isolated finite-time singularity weak enough to have only a local effect. Note that if those singular, or perhaps exceptionally sharp, events were anything but rare, they would be caught and avoided by most numerical techniques, and that identifying rare events experimentally is also hard; but it is probably true that experiments have a better chance of doing so than simulations.

Another important difference between simulations and experiments is that the latter are typically cheaper to run, at least once the initial investment is discounted, and that it is easier to rerun an experiment than to repeat a large DNS. As a consequence, experiments can scan a wider class of flows for a given effort, and they remain the method of choice when the behaviour of some simple quantity is required over a wide range of parameters. They are also able to collect more cheaply long statistical series, although, for reasons unclear to the present authors, it is often true that experimental data are noisier than numerical ones.

A characteristic of simulations is that everything is measured, and that everything can be stored and reprocessed in the future. Recent experimental techniques, such as PIV, approach the full-field capability of simulations (see the chapter by Marusic and Adrian in this volume), but the ability of DNS to create time-resolved three-dimensional fields of the three velocity components, gradients, and pressure, is still unmatched. That is an obvious advantage of simulations, but it is also responsible for their higher cost. It is no cheaper to compute the mean velocity profile of a boundary layer than to compute the whole flow field, but it is infinitely cheaper experimentally. That is one of the reasons why experiments, at least apparently, cover a wider range of Reynolds numbers than simulations. It is relatively easy to create a high-Reynolds-number flow in the laboratory, even if it is hard to measure it in detail beyond low order magnitudes such as the mean velocity, or some fluctuation intensities. Simulations, on the other hand, need to compute everything to estimate even those quantities, and the cost of increasing the Reynolds number has to be paid ‘in full’.

Even so, the Reynolds numbers of simulations have increased steadily in the past quarter century, and it is important to realize that this process is not open-ended. The goal of turbulence theory, and of the supporting simulations and experiments, should not be to reach ever increasing Reynolds numbers, but to describe turbulence well enough to be able to make useful predictions

under any circumstance. It has been understood since Kolmogorov (1941) that the key complication of turbulence is its multiscale character, and it is probably true that, if we could compile a detailed data base of the space-time evolution of enough flows with a reasonably wide range of scales, such a data base would contain all the information required to formulate a theory of turbulence. Of course, such a data set would not be a theory, but it is doubtful whether further increasing the Reynolds number of the simulations, or of the experiments, would provide much additional help in formulating one (Jiménez, 2012).

It is difficult to say a-priori when that stage will be reached, but a rough estimation is possible. The large, energy-containing, structures of wall-bounded flows are of the order of the boundary layer thickness  $\delta$  (which we will also use for the channel half-width or for the pipe radius), and the smallest near-wall viscous structures have sizes of the order of  $100\nu/u_\tau$ , where  $\nu$  is the fluid viscosity, and  $u_\tau = \tau_w^{1/2}$  is the friction velocity, defined in term of the wall shear stress  $\tau_w$ . Variables scaled with  $u_\tau$  and  $\nu$  are said to be in wall units, and will be denoted by a ‘+’ superscript. Note that, since we restrict ourselves in this chapter to incompressible flows, we will always assume the fluid density to be  $\rho = 1$ , and drop it from our equations. Capitals are used for instantaneous values, lower-case symbols for fluctuations with respect to the mean, and primes for the root-mean-squared intensities of those fluctuations. The average  $\langle \cdot \rangle$  is conceptually defined over many equivalent independent experiments, unless otherwise noted. We denote by  $x$ ,  $y$  and  $z$  the streamwise, wall-normal and spanwise coordinates, respectively, and the corresponding velocity components by  $U$ ,  $V$  and  $W$ . With this notation, the ratio between the largest and smallest scales in the flow is  $\delta^+/100$ , where  $\delta^+ = u_\tau\delta/\nu$  is the friction Reynolds number.

The channel simulations of Kim et al. (1987) had  $\delta^+ = 180$ , and therefore had essentially no scale range, but the more recent numerical channels by del Álamo et al. (2004), Abe et al. (2004) or Hoyas and Jiménez (2006), and the boundary layers by Lee and Sung (2007, 2011), Simens et al. (2009), Wu and Moin (2010), Schlatter et al. (2009); Schlatter and Örlü (2010), and Sillero et al. (2010), with  $\delta^+ \approx 1000 - 2000$ , are comparable to most well-resolved experiments, and have a full decade of scale disparity. It will be shown in §6.4 that those simulations are already providing a lot of information on the multiscale dynamics of wall-bounded flows. Moreover, because the Reynolds numbers of simulations and experiments are beginning to be comparable, it is now possible to validate, for example, the structural models derived

from experimental observations (e.g. Adrian, 2007) with the time-resolved three-dimensional flow fields of simulations, and vice versa.

It is probably true that a further factor of 5–10 in  $\delta^+$ , which would give us a range of scales close to 100, would provide us with all the information required to understand many of the dynamical aspects of wall-bounded turbulence. Using the usual estimate of  $\delta^{+3}$  for the cost of simulations, and the present rate of increase in computer speed of  $10^3$  per decade, it should be possible to compile such a data base within the next decade (Jiménez, 2003).

This brings us to discuss the question of structure versus statistics, which has been a recurrent theme in turbulence theory from its beginning. Thus, while Richardson (1920) framed the multiscale nature of turbulence in terms of ‘little and big whorls’, the older decomposition paper of Reynolds (1894) had centred solely on the statistics of the fluctuations, and proved to be more fruitful for the practical problem of turbulence modelling. Even the classical paper of Kolmogorov (1941), which is usually credited with introducing the concept of a turbulent cascade, is a statistical description of the fluctuation intensity versus scale, and it was only the slightly less famous companion paper by Obukhov (1941) that put the cascade concept in terms of interactions among eddies. It can be argued that it was not until the visualizations of large coherent structures in free-shear layers by Brown and Roshko (1974), and of sublayer streaks in boundary layers by Kline et al. (1967), that the structural view of turbulence gained modern, although still far from universal, acceptance.

This is not the place to discuss the relative merits of the two points of view, which, in any case, should be judged in relation to each particular application, but simulations have come down decisively on the side of structure. This is in part because, as we have seen, simulations are an expensive way of compiling statistics, in the same way that experiments are not very good at extracting structure, but it also points to one of the characteristic advantages of numerics, which is their ability to simulate unphysical systems.

Structural models often take a deterministic view of the flow, and deal with how its different parts interact with each other. Some of the most powerful tools for analysing interactions in physics have long been conceptual experiments, which often involve systems that cannot be physically realized, such as, for example, point masses. In simple dynamical situations, the outcome of such experiments can often be guessed correctly, and used to judge the soundness of a particular model, but in complex phenomena, such as turbulence, the guessing almost always has to be substituted by the numerical simulation of the modified system. We will see in §6.3 examples of how the

dynamics of near-wall turbulence was clarified in part through experiments of this kind, in which some of the inherent limitations of numerics, such as spatial periodicity, were put to good use in isolating what was essential, and what accidental. Similar techniques have been used for isotropic turbulent flows, which are outside the scope of the present article, but some examples can be found in Kida (1985) or She (1993).

It should be noted that conceptual experiments are not completely beyond the reach of the laboratory. For example, rough walls can be used as conceptual tests for the importance of near-wall processes in wall turbulence, since roughness destroys the detailed interactions that dominate the flow over smooth walls (Flores and Jiménez, 2006). In the same way, the use by Bradshaw (1967) of adverse pressure gradients to explore the importance of ‘inactive’ modes in boundary layers, remains one of the most beautiful examples of the experimental use of those techniques. However, the freedom afforded by numerical simulations to create artificial systems is difficult to match experimentally.

There are finally two approaches to the study of turbulence in which simulation techniques are predominant. The first one is the study of equilibrium, or otherwise simple, solutions of the Navier–Stokes equations that may be important in turbulent flows. It is generally understood that turbulence is chaotic, and it would be a surprise if a steady structure, or even a steady wave, were to be found in a natural turbulent flow. But it is also a common experience that such flows contain ‘coherent’ structures with long lifetimes. Examples range from the already cited large-scale coherent eddies of jets and shear layers, or from the sublayer streaks in wall-bounded turbulence, to the small-scale long-lived vortices in the dissipative range of many turbulent flows (Vincent and Meneguzzi, 1991; Jiménez et al., 1993). Not only are those structures believed to contribute substantially to the overall statistical properties of their respective flows but, once they are properly understood, they point to efficient control strategies (Ho and Huerre, 1984).

The prevalence of such structures raises the question of whether they can be identified with underlying solutions of the equations of motion, which are almost certain to be unstable, and therefore experimentally unobservable, but which can be extracted numerically as properties of the averaged velocity profile of the flow under study. For wall-bounded turbulence, the first solutions of this kind were obtained by Nagata (1990), and many more have been found since then. They are not only conceptually important, but their signature can be identified in full-scale turbulence (Jiménez et al., 2005). Moreover, not only the equilibrium structures, but their connections in phase space have been examined more recently, and appear to be related

to the temporal modulation of the near-wall velocity fluctuations (Halcrow et al., 2009). This approach is reviewed in §6.5.

The last interesting result of numerical experiments is the study of the possible relation between linear dynamics and the large-scale structures of turbulent flows. Turbulence is nonlinear, but a consideration of the time scales of the different processes shows that the dominant effect in the creation of the largest scales of shear flows is the energy transfer from the mean shear to the fluctuations, which is a linear process. It was understood from the beginning that the coherent eddies of free-shear layers were reflections of the Kelvin-Helmholtz instability of the mean velocity profile (Brown and Roshko, 1974; Gaster et al., 1985), but it was thought for a long time that wall-bounded flows, whose mean velocity profiles are linearly stable, could not be explained in the same way. That changed when it was realized in the early 1990's that even stable linear perturbations can grow substantially by extracting energy from the mean flow, and that it is possible to relate such 'transient' growth to the observed coherent structures in wall-bounded turbulence (Butler and Farrell, 1993; del Álamo and Jiménez, 2006). Space considerations prevent us from discussing that question here in detail, but occasional references to it will be made where appropriate.

## 6.2 The classical theory of wall-bounded turbulence

Wall-bounded turbulence includes pipes, channels and boundary layers. We will restrict ourselves to cases with little or no longitudinal pressure gradients, since otherwise the flow tends to relaminarize or to separate. In the first case it stops being turbulent, and in the second one it loses many of its wall-bounded characteristics, and tends to resemble free-shear flows. Wall-bounded turbulence is of huge technological importance. About half of the energy spent worldwide in moving fluids along pipes and canals, or vehicles through air or water, is dissipated by turbulence in the immediate vicinity of walls. Turbulence was first studied scientifically in attached wall-bounded flows (Hagen, 1839; Darcy, 1854), but those flows have remained to this day worse understood than their homogeneous or free-shear counterparts. That is in part because what is sought in both cases is different. In the classical conceptual model for isotropic turbulence, energy resides in the largest eddies, and cannot be dissipated until it is transferred by a self-similar cascade of 'inertial' eddies to the smaller scales of the order of the Kolmogorov viscous length  $\eta$ , where viscosity can act (Richardson, 1920; Kolmogorov, 1941). The resulting energy spectrum, although now recognized as only an approximation, describes well the experimental observations, not only for

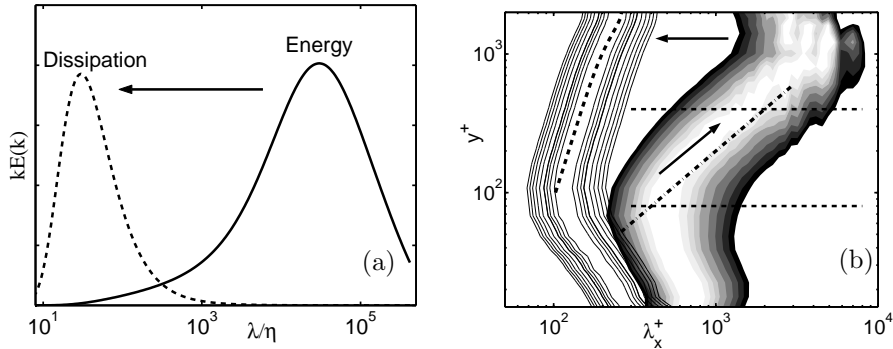


Figure 6.1 Spectral energy density,  $kE(k)$ . (a) In isotropic turbulence, as a function of the isotropic wavelength  $\lambda = 2\pi/k$ . (b) In a numerical turbulent channel with half-width  $\delta^+ = 2003$  (Hoyas and Jiménez, 2006), plotted as a function of the streamwise wavelength  $\lambda_x$ , and of the wall distance  $y$ . The shaded contours are the density of the kinetic energy of the velocity fluctuations,  $k_x E_{\mathbf{uu}}(k_x)$ . The lines are the spectral density of the surrogate dissipation,  $\nu k_x E_{\omega\omega}(k_x)$ , where  $\omega$  are the vorticity fluctuations. At each  $y$  the lowest contour is 0.86 times the local maximum. The horizontal lines are  $y^+ = 80$  and  $y/\delta = 0.2$ , and represent conventional limits for the logarithmic layer. The diagonal through the energy spectrum is  $\lambda_x = 5y$ ; the one through the dissipation spectrum is  $40\eta$ . The arrows indicate the implied cascades.

isotropic turbulence, but also for small-scale turbulence in general. A sketch can be found in Figure 6.1(a).

However, isotropic theory gives no indication of how energy is fed into the turbulent cascade. In shear flows, the energy source is the gradient of the mean velocity, and the mechanism is the interaction between that gradient and the average momentum fluxes carried by the velocity fluctuations (Tennekes and Lumley, 1972). We have already mentioned that, in free-shear flows such as jets or mixing layers, this leads to large-scale instabilities of the mean velocity profile (Brown and Roshko, 1974), with sizes of the order of the flow thickness. The resulting ‘integral’ eddies contain most of the energy, and the subsequent transfer to the smaller scales is thought to be essentially similar to the isotropic case.

In contrast, wall-bounded flows force us to face squarely the role of inhomogeneity. That can be seen in Figure 6.1(b), in which each horizontal section is the equivalent to the spectra in Figure 6.1(a) for a given wall distance. The energy is again at large scales, while the dissipative eddies are smaller, but the sizes of the energy-containing eddies change with the distance to the wall, and so does the range of scales over which the energy has to cascade. It turns out that, except very near or very far from the wall, where there are small imbalances between the production and the

dissipation of turbulent kinetic energy, most of the energy generated at a given distance from the wall is dissipated locally (Hoyas and Jiménez, 2008), but the eddy sizes containing most of the energy at one wall distance are in the midst of the inertial cascade when they are observed farther away. The Reynolds number, defined as the scale disparity between energy and dissipation at some given location, also changes with wall distance, and the main emphasis in wall turbulence is not on the local inertial energy cascade, but on the interplay between different scales at different distances from the wall.

Models for wall-bounded turbulence also have to deal with spatial fluxes that are absent from the homogeneous case. The most important one is that of momentum. Consider a turbulent channel, driven by a pressure gradient between infinite parallel planes, and decompose the flow quantities into mean values and fluctuations with respect to those means. Using streamwise and spanwise homogeneity, and assuming that the averaged velocities are stationary, the mean streamwise momentum equation is

$$\partial_x \langle P \rangle = -\partial_y \langle uv \rangle + \nu \partial_{yy} \langle U \rangle, \quad (6.1)$$

Streamwise momentum is fed across the channel by the mean pressure gradient,  $\partial_x \langle P \rangle$ , which acts over the whole cross section, and is removed by viscous friction at the wall, to where it is carried by the averaged momentum flux of the fluctuations  $-\langle uv \rangle$ . This tangential Reynolds stress resides in eddies of roughly the same scales as the energy, and it is clear from Figure 6.1(b) that the sizes of the stress-carrying eddies change as a function of the wall distance by as much as the scale of the energy across the inertial cascade. This implies that momentum is transferred in wall-bounded turbulence by an extra spatial cascade. Momentum transport is present in all shear flows, but the multiscale spatial cascade is characteristic of very inhomogeneous situations, such as wall turbulence, and complicates the problem considerably.

The wall-normal variation of the range of scales across the energy cascade divides the flow into several distinct regions. Wall-bounded turbulence over smooth walls can be described by two sets of scaling parameters (Tennekes and Lumley, 1972). Viscosity is important near the wall, and length and velocity in that region scale in wall units. There is no scale disparity in this region, as seen in Figure 6.1(b). Most large eddies are excluded by the presence of the impermeable wall, and the energy and dissipation are at similar sizes. If  $y$  is the distance to the wall,  $y^+$  is a Reynolds number for the size of the structures, and it is never large within this layer, which is typically defined at most as  $y^+ \lesssim 150$  (Österlund et al., 2000). It is conventionally

divided into a viscous sublayer,  $y^+ \lesssim 10$ , where viscosity is dominant, and a ‘buffer’ layer in which both viscosity and inertial effects have to be taken into account.

The velocities also scale with  $u_\tau$  away from the wall, because the momentum equation 6.1 requires that the Reynolds stress,  $-\langle uv \rangle$ , can only change slowly with  $y$  to compensate for the pressure gradient. This uniform velocity scale is the extra constraint introduced in wall-bounded flows by the momentum transfer. The length scale in the region far from the wall is the flow thickness  $\delta$ , but, between the inner and the outer regions, there is an intermediate layer where the only available length scale is the distance  $y$  to the wall.

Both the constant velocity scale across the intermediate region, and the absence of a length scale other than  $y$ , are only approximations. It will be seen below that large-scale eddies of size  $O(\delta)$  penetrate to the wall, and that the velocity does not scale strictly with  $u_\tau$  even in the viscous sublayer. On the other hand, Figure 6.1(b) shows that, for  $y/\delta \lesssim 0.2$ , the length scale of the energy-containing eddies is approximately proportional to  $y$ , and, if both approximations are accepted, it follows from relatively general arguments that the mean velocity in this ‘logarithmic’ layer is (Townsend, 1976)

$$\langle U \rangle^+ = \kappa^{-1} \log y^+ + A. \quad (6.2)$$

This form agrees well with experimental evidence, with an approximately universal Kármán constant,  $\kappa \approx 0.4$ , but the intercept  $A$  depends on the details of the near-wall region, because 6.2 does not extend to the wall. For smooth walls,  $A \approx 5$ . In spite of its simplicity and good experimental agreement, the theoretical argument leading to 6.2 has been challenged (Barenblatt et al., 2000) and extended (Afzal and Yajnik, 1973). For example, it is theoretically possible to include a coordinate offset inside the logarithm in 6.2, which is expected to scale roughly in wall units (Wosnik et al., 2000; Oberlack, 2001; Spalart et al., 2008). Since that question is essentially unrelated to the simulation results, it will not be pursued here, but a short critical discussion, including a reanalysis of the DNS results, can be found in Jiménez and Moser (2007).

The viscous, buffer, and logarithmic layers are the most characteristic features of wall-bounded flows, and constitute the main difference between them and other types of turbulence. Even if they are geometrically thin with respect to the layer as a whole, they are extremely important. We saw in the introduction that the ratio between the inner and the outer length scales is  $10^{-2}\delta^+$ , where the friction Reynolds number  $\delta^+$  ranges from 200 for barely

turbulent flows, to  $10^6$  for large water pipes. In the latter, the near-wall layer is only about  $10^{-4}$  times the pipe radius, but it follows from 6.2 that, even in that case, 35% of the velocity drop takes place below  $y^+ = 50$ . Because there is relatively little energy transfer among layers, except in the viscous and buffer regions, those percentages also apply to where the energy is dissipated. Turbulence is characterized by the expulsion towards the small scales of the energy dissipation, away from the large energy-containing eddies. In the limit of infinite Reynolds number, this is believed to lead to non-differentiable velocity fields. In wall-bounded flows that separation occurs not only in the scale space for the velocity fluctuations, but also in the shape of the mean velocity profile for the momentum transfer. The singularities are expelled both from the large scales, and from the centre of the flow towards the logarithmic and viscous layers near the walls.

The near-wall viscous layer is relatively easy to simulate numerically because the local Reynolds numbers are low, and difficult to study experimentally because it is usually very thin in laboratory flows. Its modern study began experimentally in the 1970's (Kline et al., 1967; Morrison et al., 1971), but it got its strongest impulse with the advent of high-quality direct numerical simulations in the late 1980's and in the 1990's (Kim et al., 1987). We will see in the next section that it is one of the turbulent systems about which most is known.

Most of the velocity difference that does not reside in the near-wall viscous region is concentrated just above it, in the logarithmic layer, which is also unique to wall turbulence. It follows from 6.2 that the velocity difference above the logarithmic layer is about 20% of the total when  $\delta^+ = 200$ , and that it decreases logarithmically as the Reynolds number increases. In the limit of very large Reynolds numbers, all the velocity drop is in the logarithmic layer.

The logarithmic layer is intrinsically a high-Reynolds number phenomenon. Its existence requires at least that its upper limit should be above the lower one, so that  $0.2\delta^+ \gtrsim 150$ , and  $\delta^+ \gtrsim 750$ . The local Reynolds numbers  $y^+$  of the eddies are also never too low. The logarithmic layer has been studied experimentally for a long time, but numerical simulations with even an incipient logarithmic region have only recently become available. It is worse understood than the viscous layers, and will be reviewed in §6.4.

### 6.3 The dynamics of the near-wall region

The region below  $y^+ \approx 100$  is dominated by coherent streaks of the streamwise velocity and by quasi-streamwise vortices. The former are an irregular

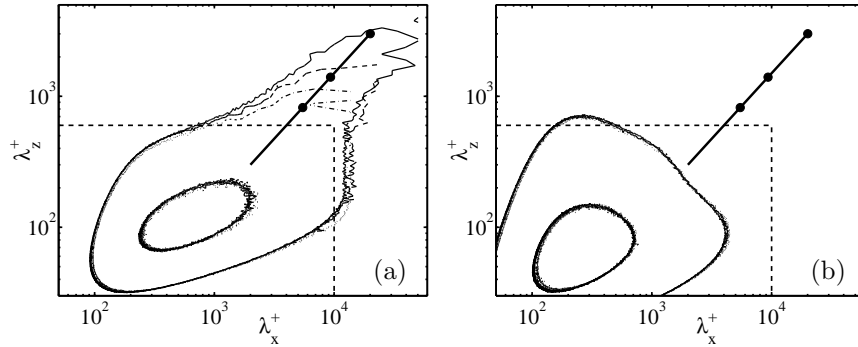


Figure 6.2 Two-dimensional spectral energy density  $k_x k_z E(k_x, k_z)$  in the near-wall region ( $y^+ = 15$ ), in terms of the streamwise and spanwise wavenumbers. Numerical channels,  $\cdots$ ,  $\delta^+ = 547$  (del Álamo and Jiménez, 2003);  $---$ , 934 (del Álamo et al., 2004);  $---$ , 2003 (Hoyas and Jiménez, 2006). Spectra are normalized in wall units, and the two contours for each spectrum are 0.125 and 0.625 times the maximum of the spectrum for the highest Reynolds number. The heavy straight line is  $\lambda_z = 0.15\lambda_x$ , and the heavy dots are  $\lambda_x = 10\delta$  for the three cases. The dashed rectangle is the spectral region used in Figure 6.3(a) to isolate the near-wall structures. (a) Kinetic energy. (b) Enstrophy,  $|\omega|^2$ .

array of long ( $x^+ \approx 10^3$ – $10^4$ ) sinuous alternating streamwise jets superimposed on the mean shear, with an average spanwise separation of the order of  $z^+ \approx 100$ . The quasi-streamwise vortices are slightly tilted away from the wall, and stay in the near-wall region only for  $x^+ \approx 100$  (Moin and Moser, 1989). Several vortices are associated with each streak (Jiménez et al., 2004), with a longitudinal spacing of the order of  $x^+ \approx 300$ .

The streaks and the vortices are easily separated in the two-dimensional spectral densities in Figure 6.2, which are taken at the kinetic energy peak near  $y^+ = 15$ . The streaks are represented by the spectra of the kinetic energy in Figure 6.2(a), which are dominated by the streamwise velocity. The vortices are represented by the enstrophy spectra in Figure 6.2(b), which are very similar to those of the wall-normal velocity at this distance to the wall. The three spectra in each figure correspond to turbulent channels at different Reynolds numbers, and differ from one another almost exclusively in the long and wide structures in the upper-right corner of the kinetic energy spectra, with sizes of the order of  $\lambda_x \times \lambda_z = 10\delta \times 1.5\delta$ . A rectangle with these dimensions has been added to Figure 6.4, where the large-scale modulation of the flow can be easily seen.

In this section, we deal mostly with the rotational structures in the spectral region in which  $\lambda_x^+ \lesssim 10^4$  and  $\lambda_z^+ \lesssim 600$ . Figure 6.3(a) shows that, when the statistics are computed within that window, they are essentially indepen-

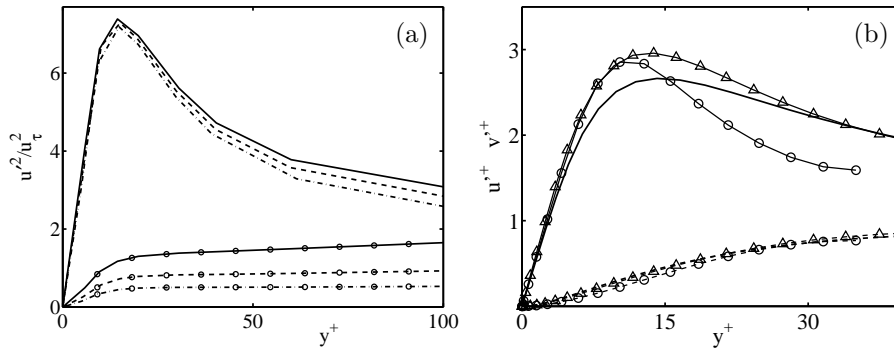


Figure 6.3 Profiles of the velocity fluctuations. (a) Squared intensities of the streamwise velocity. Simple lines are computed within the spectral window  $\lambda_x^+ \times \lambda_z^+ = 10^4 \times 600$ ; those with symbols are outside that window. Lines and conditions as in Figure 6.2. (b) Root-mean-squared intensities. Simple lines are a full channel with  $\delta^+ = 180$  (Kim et al., 1987);  $\text{---}\triangle\text{---}$ , a minimal channel with  $\delta^+ = 180$  (Jiménez and Moin, 1991);  $\text{---}\circ\text{---}$ , a permanent-wave autonomous solution (Jiménez and Simens, 2001).  $\text{---}$ , streamwise velocity;  $\text{---}$ , wall-normal velocity.

dent of the Reynolds number, especially below  $y^+ \approx 100$ . The larger-scale structures outside the window become stronger as the Reynolds number increases, and contain no enstrophy or tangential Reynolds stresses at this wall distance. They extend into the logarithmic layer, where they are both rotational and carry stresses (Hoyas and Jiménez, 2006), and correspond to the ‘inactive eddies’ of Townsend (1961). They will be discussed in §6.4. In this part of the flow, they are responsible for the growth of the turbulent energy with the Reynolds number (deGraaff and Eaton, 2000).

Note that, even within the rotational region, the longer end of the spectrum is also wider. It was shown by Jiménez et al. (2004) that this is mostly due to meandering of the structures, and that even the longest near-wall low-velocity streaks are seldom wider than  $\Delta z^+ = 50$ . We will see below that this is also the order of magnitude of the height of those streaks, which are therefore roughly equilateral wavy cylinders. Meandering, as well as a certain amount of branching, is easily seen in the top panel of Figure 6.4 and in Figure 6.6(e), and has been documented in the logarithmic layer by Hutchins and Marusic (2007).

Soon after they were discovered by Kline et al. (1967), it was proposed that the streaks and the vortices were involved in a regeneration cycle in which the vortices are the results of an instability of the streaks (Swearingen and Blackwelder, 1987), while the streaks are caused by the advection of the mean velocity gradient by the vortices (Bakewell and Lumley, 1967). Both processes have been documented and sharpened by numerical experi-

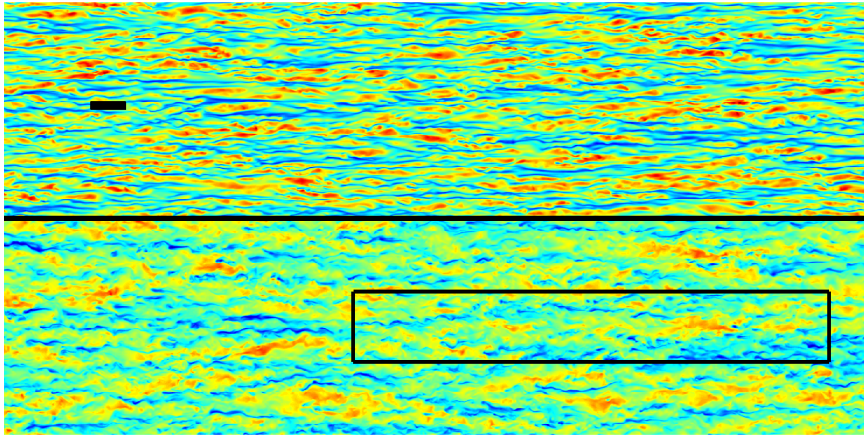


Figure 6.4 Streamwise velocity in wall-parallel planes. The top panel is at  $y^+ = 12$ , and the bottom one at  $y^+ = 50$ . Channel at  $\delta^+ = 547$  (del Álamo and Jiménez, 2003). The flow is from left to right, and each panel is approximately  $10^4$  by  $5 \times 10^3$  wall units. The velocity range in the top panel is  $U^+ = 0.6$ –17 (blue to red), and in the bottom one, 10–26. The small black rectangle in the top panel is a minimal box, of size  $400 \times 100$  wall units. The one in the lower panel is  $10\delta \times 1.5\delta$ .

ments. For example, Jiménez and Pinelli (1999) showed that disturbing the streaks inhibits the formation of the vortices, but only if it is done between  $y^+ \approx 10$  and  $y^+ \approx 60$ , suggesting that it is predominantly between those limits where the regeneration cycle works. There is a substantial body of numerical (Hamilton et al., 1995; Waleffe, 1997; Schoppa and Hussain, 2002) and analytic (Reddy et al., 1998; Kawahara et al., 2003) work on the linear instability of model streaks. The inflection points of their distorted velocity profiles are unstable to sinuous perturbations, and the eigenfunctions closely resemble the shape and location of the observed vortices. The model implied by these instabilities is a cycle in which streaks and vortices are created, grow, generate each other, and eventually decay (see Jiménez and Pinelli, 1999, for additional references).

Although the flow in the buffer layer is disorganized and seemingly chaotic, the spatial chaos is not required to reproduce the turbulence statistics. Jiménez and Moin (1991) presented simulations in which the near-wall region was substituted by an ordered ‘crystal’ of surprisingly small identical ‘minimal’ units, of size  $400 \times 100$  wall units in the streamwise and spanwise directions. A box of that size is superimposed on the top panel of Figure 6.4. Each unit contains a single streak that crosses the box (and is therefore essentially infinite), and, on average, a single pair of staggered quasi-streamwise vortices, in spite of which it reproduces fairly well the statistics of

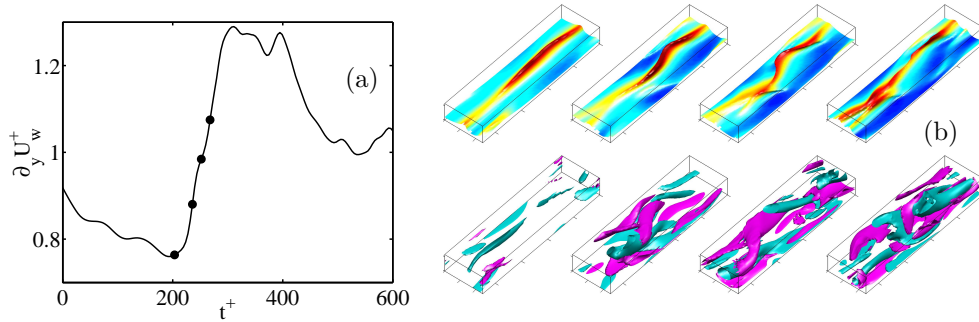


Figure 6.5 Evolution of a minimal Poiseuille flow during a bursting event.  $L_x^+ \times \delta^+ \times L_z^+ = 460 \times 180 \times 125$ . (a) Evolution of the mean velocity gradient at the wall. The dots correspond to the snapshots on the right. (b) The top frames are isosurfaces  $U^+ = 8$ , coloured by the distance to the wall, up to  $y^+ = 30$  (blue to red). The bottom ones are  $\omega_x^+ = 0.2$  (purple), and  $-0.2$  (cyan). The flow is from bottom-left to top-right, and time marches towards the right. The top of the boxes is  $y^+ = 60$ , and the axes move with velocity  $U_a^+ = 7.6$ .

the full flow (Figure 6.3b). Moreover, it was shown by Jiménez and Pinelli (1999), that the dynamics of the layer below  $y^+ \approx 60$  is autonomous, in the sense that the streaks and the vortices continue regenerating themselves even when the flow above them is artificially removed, and that those local interactions still result in approximately correct statistics.

Even further removed from the real flow are the three-dimensional nonlinear equilibrium solutions of the Navier–Stokes equations discussed in §6.5, which were first obtained numerically at about the same time as the minimal units just mentioned. Their fluctuation intensity profiles, included in Figure 6.3(b), are also strongly reminiscent of experimental turbulence.

On the other hand, although its statistics are well approximated by those steady solutions, the real flow is not steady. The time evolution of the near-wall structures is most easily studied in minimal boxes, because each of them contains only a few structures whose evolution can be traced by integral measures over the whole box. All those measures ‘burst’ quasi-periodically on times of the order of  $T^+ = Tu_\tau^2/\nu \approx 400$  (Jiménez and Moin, 1991; Hamilton et al., 1995; Jiménez et al., 2005). An example is given in Figure 6.5, which depicts the rising phase of a burst. The streak becomes wavy, friction increases sharply, and the streamwise vorticity grows. It is harder to follow the time evolution of individual structures in real flows, but when their statistics are compiled over randomly chosen sub-boxes of ‘minimal’ size, their distributions agree well with those of the temporal variability of the minimal flows (Jiménez et al., 2005), suggesting that full flows also burst.

The period given above is longer than the survival time of individual vortices, which decay viscously with a characteristic time  $T^+ \approx 60$  if their production is artificially inhibited by damping the streaks (Jiménez and Pinelli, 1999). A similar time scale,  $T^+ \approx 50$ , can be extracted from the space-time spectra of the wall-normal velocity in natural flows (del Álamo et al., 2006). The discrepancy between the vortex lifetimes and the bursting period suggests that the regeneration cycle consists of a relatively quiescent phase followed by shorter eruptions. Jiménez et al. (2005) analysed several minimal flows, and concluded that the bursting phase takes about one-third of the cycle, or  $T^+ \approx 100$ , half of which is taken by the growth of the instability, and the other half by its decay.

It is likely that the quasi-periodic bursting of the minimal boxes is an artefact of the spatial periodicity, and that the streaks in the real flow move away from the location where they are created before bursting again. In a minimal periodic flow, the spatial periodicity brings the streak back into the simulation box but, in a real one, bursts would be more or less independent of each other. All that probably remains is the average time elapsed from the moment in which a burst creates a vortex and begins to form a streak, until the streak becomes unstable and erupts into a new burst. That time is presumably related to the growth rate of the instabilities of the streak itself, which is proportional to its internal velocity gradient, of the order of  $u_\tau/\Delta z$ . The implied growth times,  $T^+ = O(\Delta z^+)$ , are about a hundred wall units, compatible with the bursting times mentioned above. Note that the approximate agreement of those orders of magnitude is unlikely to be a coincidence, and should rather be seen as determining the size of the streaks. Schoppa and Hussain (2002) noted that the streaks found in real flows are typically stable, or at most marginally unstable, and the likeliest interpretation of that observation is that the streaks grow until they become unstable, after which they burst, and are quickly destroyed. On the other hand, the viscous decay time of the streak is  $T^+ = O(\Delta z^{+2}) = O(3000)$ , much longer than the bursting period, suggesting again that the length of the streaks is determined by their instabilities, rather than by their viscous decay.

The streaks are wakes created in the mean velocity profile as the vortices are advected and sheared. For example, Jiménez et al. (2004) studied the relation between streaks and vortices using as surrogates connected regions in which  $u$  or  $v$  were more than one standard deviation away from their means in planes parallel to the wall. Two such objects were considered related if their rectangular bounding boxes intersected. Figure 6.6(a) shows the probability density functions (PDFs) of the position of the  $v > v'$  ejections with

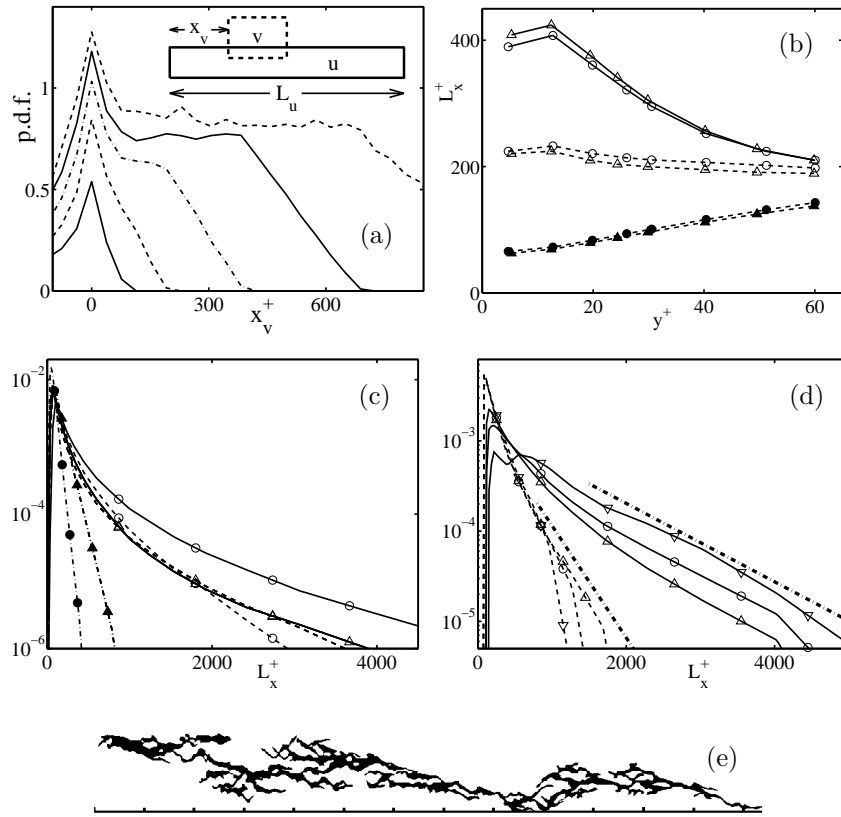


Figure 6.6 Numerical channels as in Figure 6.2. (a) Compensated PDF,  $L_u p(x_v | L_u)$ , of the positions of the front ends of the bounding boxes of  $v > v'$  ejections with respect to the front-end of the low-velocity streaks they intersect, for several bands of streak lengths, limited by  $L_u^+ = 50, 100, 200, 400, 700, 1100$ . Channel with  $\delta^+ = 2003$  and  $y^+ = 13$ . Longer PDFs correspond to longer streaks. (b) Average lengths of the bounding boxes of strong velocity fluctuations, as functions of  $y$ . Lines with open symbols are  $|u| \geq u'$ . —, Low-velocity; ----, high-velocity. Lines with closed symbols are  $|v| \geq v'$ .  $\circ$ ,  $\delta^+ = 934$ ;  $\triangle$ , 2003. (c) PDFs of the lengths of the velocity perturbations. Lines as in (b), but  $\circ$ ,  $y^+ = 13$ ;  $\triangle$ ,  $y^+ = 50$ .  $\delta^+ = 2003$ . (d) PDFs of the lengths of the  $u$ -boxes, restricted to the band  $13 \leq y^+ \leq 50$ . Lines as in (b), but  $\nabla$ ,  $\delta^+ = 547$ ;  $\circ$ , 934;  $\triangle$ , 2003. The heavy chaindotted lines are exponentials with  $L_c^+ = 350$  and  $10^3$ . (e) Long sublayer streak, defined as a connected region in the plane  $y^+ = 13$  for which  $u < -u'$ , in a channel at  $\delta^+ = 2003$ . The tick marks in the streamwise ( $x$ ) axis are 1000 wall units apart.

respect to the head of the streak to which they are related, as functions of the streak length. The ejections are uniformly distributed along the streaks, except at the streak head, which is always more likely to have an ejection.

If, in this wake model, we assume an advection velocity  $U_{ad}^+ \approx 8$  near the wall (Kim and Hussain, 1993), the vortices would create streaks of length

$L_x^+ \approx 800$  before decaying, which is consistent with the spectral maximum in Figure 6.2(a). Moreover, the ratio (one to three) between the active lifetimes of the bursts and the full regeneration period suggests that there should be a similar ratio between active and total lengths along the streaks, which is also roughly correct. The mean length of the vortices, as measured by the regions of high wall-normal velocity in the buffer layer, is approximately 80 wall units (Figure 6.6b), while we have already seen that their mean spacing along the streaks is of the order of  $\lambda_x^+ = 300$ .

Figure 6.6(b) shows that the character of the streaks changes around  $y^+ \approx 30\text{--}40$ , which is also where viscosity stops being an important dynamical factor for the energy-containing eddies (Jiménez et al., 2004). Figure 6.6(c) shows the PDFs of the lengths of the streaks ( $u$ ) and vortices ( $v$ ) in two planes at different distances from the wall. In the viscous region,  $y^+ = 12$ , the average length of low-speed streaks,  $L_x^+ \approx 500$ , is about twice that of the high-speed ones, but they shorten away from the wall, and settle to  $L_x^+ \approx 250$  beyond  $y^+ = 50$ . Above that height, the lengths of the two types of streaks are essentially the same and, at least at the Reynolds number of Figure 6.6(c), the longest streaks are the low-velocity ones in the viscous layer. The simplest explanation is that the high-velocity regions have a higher velocity gradient at the wall, and, being associated with downwashes, are not as tall as the low-velocity ones. The viscous dissipation is proportional to the square of the velocity derivatives, and, at  $y^+ \approx 10$ , it is predominantly due to the wall-normal gradients. Thus, although there is very little asymmetry between the streaks of both signs regarding the wall-parallel velocity gradients, the dissipation due to the wall-normal ones is much higher in the thinner fast streaks than in the taller low-speed ones. That asymmetry weakens as the effect of viscosity decreases away from the wall, and the two velocity signs then behave similarly. The disappearance of the long streaks above the viscous region can also be seen in the spectral densities shown in Figure 6.8(a), in the next section, which correspond to the logarithmic layer, but which includes the kinetic-energy spectrum at  $y^+ = 15$ , for comparison. Even at the relatively high Reynolds number of this figure, which would tend to reinforce the larger structures of the outer region, the energy in  $\lambda_x^+ \times \lambda_z^+ \approx 10^4 \times 100$  has disappeared at  $y^+ = 100$ , and the remaining long structures seem to belong to the logarithmic-layer family. The same distinction is clear in Figure 6.4. The streaks in the upper panel, at  $y^+ = 12$ , are mostly absent from the lower one, at  $y^+ = 50$ , and the longest structures at the higher level are wider and more disorganized. On the other hand, the positive and negative  $v$ -structures, corresponding to

the vortices, have lengths similar to each other, and both grow longer away from the wall.

The viscous low-velocity streaks are not only long in the mean, but the PDF of their lengths has a very long superexponential tail, which can only be explained by the interaction of several bursts. A plausible model for that interaction is suggested by Figure 6.6(d). It was shown by del Álamo et al. (2006) that the largest vortical structures at each wall distance are objects that remain attached to the wall even when they extend far into the flow (Townsend, 1961), and that they are associated with long low-velocity features. Consequently, part of the reason why the PDFs in Figure 6.6(c) are long is that they include the roots of taller objects that do not really belong to their wall distance. In an attempt to separate those roots from the PDFs of objects which are local to the viscous region, we display in Figure 6.6(d) the difference between the histograms at the planes  $y^+ = 12$  and  $y^+ = 50$ . The long low-speed streaks of the viscous layer still appear, but their PDF is now a fairly good exponential, with a characteristic length  $L_c^+ \approx 1000$ , which is the same for the three Reynolds numbers in the figure. The distributions of the high-velocity streaks are also exponential, but with a shorter length scale,  $L_c^+ \approx 250$ . Exponential probability distributions suggest a Poisson process (Feller, 1971), which can be incorporated into several plausible models for the viscous region.

The simplest one is that streaks grow by the aggregation of smaller units. Consider elementary streaks created by individual bursts with average length  $L_0$ , and assume that each such unit has a probability  $q < 1$  of connecting with another one, either by chance, or by creating a new burst in its wake. The probability of a composite streak of  $n \geq 1$  units is  $p(n) = (1 - q)q^{n-1}$ , which can be written in terms of the streak length,  $L = nL_0$ , as  $p(L) \sim \exp(-L/L_c)$  for  $L \geq L_0$ , where  $L_c = -L_0/\log(q)$ . The two factors entering  $L_c$  can be separated if we take into account that the PDF peaks at  $L = L_0$ , in which case the best fit to Figure 6.6(d) is approximately  $L_0^+ \approx 500$  and  $q \approx 0.6$ . Those are sensible numbers, given the previous discussion on the effects of a single burst, and they are given some credence by the appearance of the long streaks, such as the one in Figure 6.6(e), but they should be used with care because the subtraction method used to generate Figure 6.6(d) is hard to justify for the very short events near the mode of the PDF. For example, note that the shortest streaks around  $L_0$  become more frequent as the Reynolds number increases, causing a systematic lowering of the offset of the exponential tails. Moreover, an equally valid model would be that streaks tend to form infinitely long networks, but are cut randomly by some external influence, presumably from the logarithmic or outer layers. The

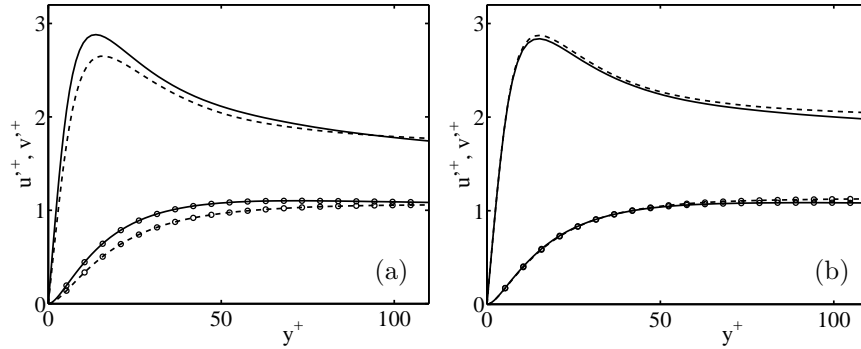


Figure 6.7 Fluctuation intensities computed over sub-boxes with dimensions  $\lambda_x \times \lambda_z = 1.5\delta \times 0.75\delta$ . Numerical channel at  $\delta^+ = 2003$  (Hoyas and Jiménez, 2006). Simple lines are  $u'$ , and those with symbols are  $v'$ , conditioned to boxes in which the friction velocity is more than one standard deviation above (—) or below (---) average. (a) Wall distance and velocities normalized with the global friction velocity. (b) Normalized with the friction velocity local to each sub-box.

two models give identical length distributions, and can probably only be distinguished by a full space-time analysis of this region of the flow.

It is interesting that the PDFs of the lengths of the  $v$ -events, which represent the vortices, are also exponential, although with a shorter length scale  $L_c^+ \approx 200$  near the wall, suggesting that they also form packets. Although this is reminiscent of the experimental observations of vortex packets in the logarithmic region (Adrian, 2007), the difference in length scales makes it unlikely that the two phenomena are directly related.

There is an obvious large-scale modulation in the near-wall panel of Figure 6.4, on scales that we have associated with the outer layer. Mathis et al. (2009) discussed that modulation, and concluded that it is stronger than a simple linear superposition of the velocity of the different spectral modes. It turns out that most of it can be absorbed into the variability of the local friction velocity, which changes from place to place because of the effect of large-scale down- and up-drafts. That can be seen in Figure 6.7, which displays velocity statistics compiled over sub-boxes of sizes comparable to the outer structures. The standard deviation for each sub-box is computed with respect to the average velocity over that sub-box, and the boxes are classified according to their mean friction velocity, which varies with respect to the global mean by about  $\pm 5\%$ . Not surprisingly, boxes with high friction velocities correspond to mean downdrafts, and those with low friction velocities to updrafts, with maximum differences of the wall-normal velocity averaged over the sub-box,  $\langle v \rangle^+ \approx 0.1$ , peaking at  $y/\delta \approx 0.2$ . Figure 6.7(a)

compares statistics over boxes whose friction velocities are more than one standard deviation above or below the global mean. The former are more intense than the latter, but most of the difference can be compensated by normalizing both the velocities and the wall distance with the local mean friction velocity averaged over the box, as in Figure 6.7(b). That makes sense, because the boxes, which at the Reynolds number of the simulation are  $3000 \times 1500$  wall units long and wide, are much larger than the elementary structures of the viscous layer, which therefore ‘live’ in an environment defined by the mean box properties (Jiménez, 2012).

In summary, our best understanding of the viscous and buffer layers is, at present, that the peak of the energy spectrum, at  $\lambda_x^+ \times \lambda_z^+ = 1000 \times 100$ , is associated with structures that can be approximated by the steady travelling-wave solutions of the Navier-Stokes equations discussed in §6.5, but which in reality undergo strong quasi-periodic bursting. The bursts create vortices whose wakes are elemental streaks with lengths of the order of 1000 wall units, and which aggregate into the longer observed composite objects, either by chance or by generating new bursts in their tails. Those structures are restricted to  $y^+ \lesssim 50$ , which is the only part of the flow in which high- and low-velocity streaks are substantially different from each other. They give way above that level to more symmetric velocity fluctuations, in which viscosity is not the determining factor.

#### 6.4 The logarithmic and outer layers

Immediately above the viscous region we find the logarithmic and outer layers. They are expensive to compute, and the first simulations with even an incipient logarithmic region have only recently began to appear. For example, the logarithmic layer in the numerical channel in Figure 6.1(b) is defined as the range,  $y^+ = 80$  to 400, in which the wavelength of the spectral energy peak grows linearly with  $y$ , and only spans a factor of five. Even so, those simulations, as well as the simultaneous advances in experimental methods reviewed by Marusic and Adrian (2012) in this volume, have greatly improved our knowledge of the kinematics of the outer-layer structures, and are beginning to give some indications about their dynamics.

Before considering those results, it should be stressed that structural models mean something different for the outer and buffer layers. Near the wall, the local Reynolds numbers are low, and the structures are smooth, and it is possible to speak of ‘objects’, and to write equations for them. Both things are harder above the buffer layer. The integral scales are  $O(y)$ , the velocity fluctuations are  $O(u_\tau)$ , and the turbulent Reynolds number is

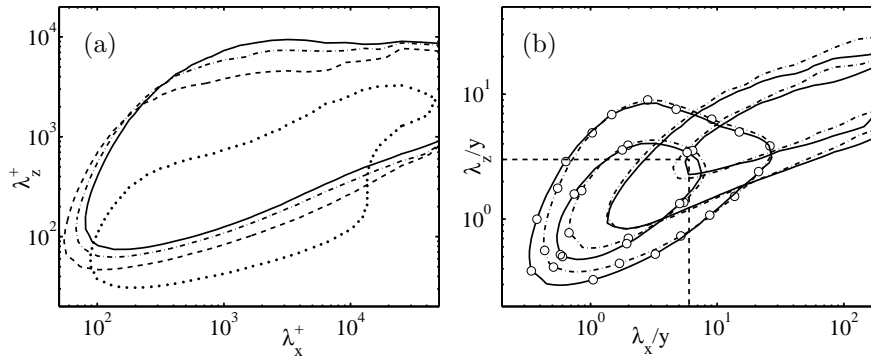


Figure 6.8 (a) Spectral densities of the kinetic energy in the logarithmic region of a numerical channel at  $\delta^+ = 2003$ , versus wavenumbers scaled in wall units. Isolines are 0.125 times the maximum of each spectrum.  $\cdots$ ,  $y^+ = 15$ ;  $---$ , 100;  $- \cdot -$ , 200;  $---$ , 300. (b) Two-dimensional spectral densities of  $u$  (without symbols) and  $v$  (with symbols), versus wavenumbers scaled with the wall distance. Lines as in (a). The dashed rectangle is  $(\lambda_x, \lambda_z) = (6, 3)y$ . Isolines are 0.3 and 0.6 times the maximum of each spectrum.

$Re = O(u_\tau y / \nu \equiv y^+)$ . The definition of the outer layers,  $y^+ \gg 1$ , implies that most of their structures have large internal Reynolds numbers, and are themselves turbulent. The energy-containing eddies have cascades connecting them to the dissipative scales, and algebraic spectra that correspond to non-smooth geometries. They are ‘eddies’, rather than ‘vortices’, because turbulent vorticity is always at the viscous Kolmogorov length scale, separated from the energy-containing scales by a ratio  $Re^{3/4}$ . Some examples are given in Figure 6.9. We can only expect dynamical descriptions of those structures in a statistical sense, perhaps coupled to stochastic models for the turbulent cascade ‘underneath’.

Perhaps the first new information provided by the numerics about the logarithmic layer was spectral, although some of the early analyses of large-eddy simulations of channels contributed significantly to the understanding of the bursting event (Kim, 1985). Very large scales had been found experimentally in the outer layers of turbulent wall flows (Jiménez, 1998; Kim and Adrian, 1999), but DNS provided the first data about their two-dimensional spectra, and about their wall-normal correlations (del Álamo and Jiménez, 2003; del Álamo et al., 2004). Figure 6.8(a) shows that the spectral densities of the kinetic energy in the logarithmic region have elongated shapes along lines  $\lambda_z^2 \sim y \lambda_x$ , which del Álamo and Jiménez (2003) interpreted as the signature of statistically conical structures similar to the ‘attached’ eddies proposed by Townsend (1976). Note that this description only holds above  $y^+ \approx 100$ .

As mentioned in the previous section, the buffer-layer spectrum in Figure 6.8(a) is dominated by streaks with  $\lambda_z^+ \approx 100$ , but they have essentially disappeared at  $y^+ = 100$ . The vorticity is isotropic above that height, with the three components centred around 40 Kolmogorov viscous units (Figure 6.1b), but the large-scale velocities are very anisotropic, with the long structures mostly associated with the streamwise component (Figure 6.8b).

Figures 6.8(a) and 6.8(b) show that the cores of the velocity spectra scale relatively well with the wall distance, although, as in all turbulent flows, their short wavelengths scale with the Kolmogorov viscous length, and the long- and wide-wavelength limits of the streamwise velocity scale with the channel height. The velocities below  $\lambda_x^+ \approx 500$  are essentially isotropic (not shown), with similar intensities for the three components. Note that the scaling with  $y$  of the wavelengths in Figure 6.8(b) can be read as meaning that the structures that reach from the wall to height  $y$  are not much longer than  $6y$  in the logarithmic layer. Longer structures are also taller. We will see later that the dashed rectangle in Figure 6.8(b) represents the minimal box that can sustain turbulence up to a given  $y$ , presumably because it is able to contain at least one complete structure with that height.

Indeed, when three-dimensional flow fields eventually became available from simulations, it was found that there is a self-similar hierarchy of compact ejections extending from the buffer layer into the outer flow, within which the coarse-grained dissipation is more intense than elsewhere (del Álamo et al., 2006). An example is shown in Figure 6.9(a). They correspond to the ejections represented by the  $v$ -spectra in Figure 6.8(b), and, when the flow is conditionally averaged around them, as in Figure 6.9(b), they are associated with extremely long, conical, low-velocity regions whose intersection with a fixed  $y$  is a parabola that explains the quadratic behaviour of the spectrum of  $u$ . These are probably the same objects variously described as VLSM or “superstructures” in the paper by Marusic and Adrian (2012) in this volume, and are not just statistical constructs. Individual cones are observed as low-momentum ‘ramps’ in streamwise sections of instantaneous flow fields (Meinhart and Adrian, 1995), and two examples can be seen in the instantaneous streamwise velocity isosurface in Figure 6.9(c). As in the buffer layer, the longest low-velocity structures at each height appear to be composite objects, formed by the concatenation of smaller subunits of dimensions of the order of the  $v$ -ejections mentioned above (Figure 6.9d). We have seen that their near-wall footprints are seen in the spectra of the buffer layer as the ‘tails’ in Figure 6.2(a).

When the cones reach heights of the order of the flow thickness, they stop growing, and become long cylindrical ‘streaks’, similar to those of the

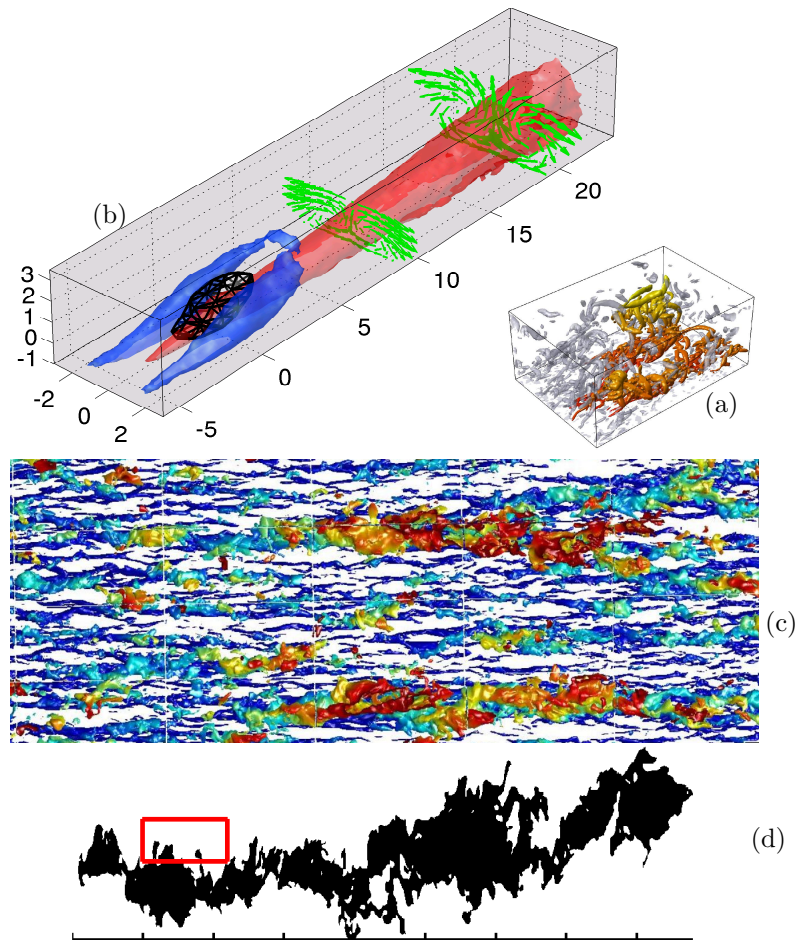


Figure 6.9 (a) The coloured object is a cluster of connected vortices in a  $\delta^+ = 550$  channel (del Álamo and Jiménez, 2003), from red near the wall, to yellow near  $y = \delta$ . Grey objects are unconnected vortices. (b) Averaged velocity field conditioned to a vortex cluster. The black mesh is an isosurface of the PDF of the vortex positions. The blue volume surrounding the cluster is the isosurface  $u^+ = 0.3$ , and the red one downstream is the isosurface  $u^+ = -0.1$ . The vector plots represent  $(v, w)$  in the planes  $r_x/y_c = 10, 20$  (from del Álamo et al., 2006). (c) Isosurface of the streamwise fluctuation velocity,  $u^+ = -2$ , in a computational channel with  $\delta^+ = 550$ . The flow is from left to right, in a partial domain  $(15.5 \times 5.5) \delta$  in the streamwise and spanwise directions. Colours are distance from the wall, from blue at the wall, to red at the central plane. Figures (a) and (c), courtesy of O. Flores. (d) Long logarithmic-layer streak, defined as a connected region in the plane  $y^+ = 200$  for which  $u < -u'$ , in a channel at  $\delta^+ = 2003$ . The tick marks in the streamwise ( $x$ ) axis are 1000 wall units apart, and the red box is  $(6, 3)y$ .

sublayer, but with spanwise scales of about  $1-2\delta$ . They are fully turbulent objects, and neither simulations nor experiments have provided hard

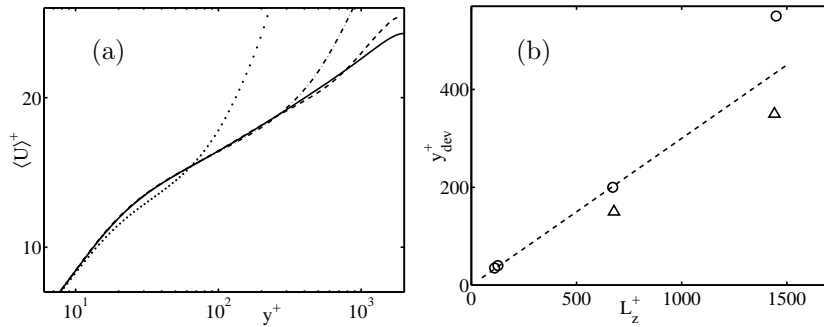


Figure 6.10 (a) Mean profiles of small-box simulations, compared with a full-box one.  $\delta^+ \approx 1800$ .  $\cdots\cdots$ ,  $L_x^+ \times L_z^+ = 440 \times 110$ ;  $-\cdot-\cdot-$ ,  $1350 \times 670$ ;  $-----$ ,  $2900 \times 1450$ ;  $————$ , full. (b) Height of the logarithmic profile in small-box simulations, as a function of the spanwise box dimension. The open circles are the cases in (a). The two symbols at  $L_z^+ \approx 100$  have  $\delta^+ = 180$  and  $1800$ . The triangles are as in (a), but with shorter or longer boxes,  $770 \times 1440$  and  $2700 \times 680$ . The dashed line is  $y_{dev} = 0.3L_z$ .

estimates of their maximum length, although the longest available spectra suggests lengths of about  $25\delta$  (Jiménez and Hoyas, 2008). The wall-normal dimension of these ‘global modes’ is of the order of the flow thickness, and they extend from the central plane to the wall (del Álamo and Jiménez, 2003; del Álamo et al., 2004). The probability density functions of the velocity strongly suggest that these large scales account for the variation of the turbulence intensities with the Reynolds number, both near and far from the wall (Jiménez and Hoyas, 2008), both of which disappear when wavelengths longer than about  $6\delta$  are filtered from the flow field (Jiménez, 2007).

It is interesting that the logarithmic layer can also be simulated in relatively small numerical boxes, periodic in the two wall-parallel directions (Flores and Jiménez, 2010). Those boxes are not minimal in the sense of those discussed in §6.3 for the buffer layer. When the simulation box is made smaller, turbulence does not decay, but becomes restricted to a thinner layer near the wall. In that sense, the minimal boxes of Jiménez and Moin (1991) are the innermost members of a hierarchy in which progressively smaller wall-attached structures are isolated in progressively smaller numerical boxes. The especial feature of the minimal boxes of the buffer layer is that they cannot be restricted any further, while larger boxes isolate more complicated structures, fully multiscale, that reach from the wall farther into the core flow.

That can be seen in Figure 6.10(a), which compares the mean velocity profiles of three numerical channels with different periodic box sizes to the profile of a full channel, all at the same nominal Reynolds number. The

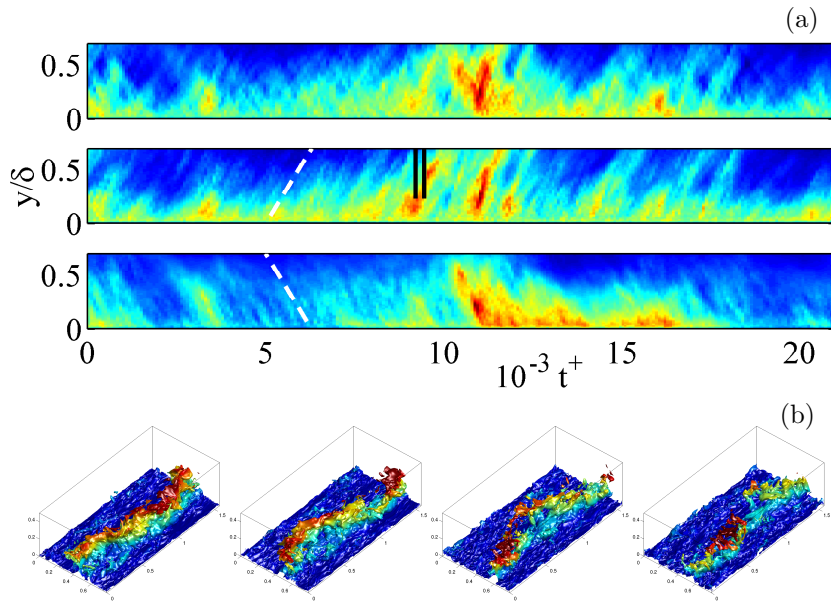


Figure 6.11 (a) Temporal evolution of the Reynolds stress,  $-\langle uv \rangle$  for a small-box simulation,  $\delta^+ = 1800$ ,  $L_x^+ = 2900$ ,  $L_z^+ = 1450$ . In the top panel,  $\langle uv \rangle$ , is averaged over each wall-parallel plane; in the central one, it is averaged only over events for which  $(u < 0, v > 0)$ , and in the bottom one, for  $(u > 0, v < 0)$ . The heavy dashed lines are  $dy/dt = \pm u_\tau$ . (b) Time evolution of the  $U^+ = 15$  isosurface during the burst marked by the two vertical lines in the middle panel of (a). Colours are distance from the wall, with a maximum (red)  $y/\delta \approx 0.4$ . The flow is from bottom-left to top-right, and time increases towards the right (from Flores and Jiménez, 2010).

smallest box corresponds to the minimal dimensions in §6.3, and its profile diverges just above the buffer layer. The other two, with larger boxes, reproduce well the logarithmic profile over taller regions. If we arbitrarily define the limit of healthy turbulence as the point where the mean profiles begin to diverge from that of a full-sized flow, it turns out to be roughly proportional to the box size. The critical dimension appears to be the spanwise periodicity,  $y_{dev} \approx 0.3L_z$ , as seen in Figure 6.10(b), which includes the three cases in Figure 6.10(a), plus other combinations in which one of the box dimensions was doubled or halved independently of the other one. This result agrees with the early experiments of Toh and Itano (2005), who were able to simulate a healthy logarithmic profile in a numerical channel with a fairly wide box, but whose streamwise dimension was of the order of the buffer-layer minimal boxes ( $L_z^+ = 380 \approx \delta^+$ ).

As in the case of the buffer layer, small-box simulations can be used to study the dynamics of the elementary energy-containing structures of the

logarithmic layer. They also contain a single large-scale streamwise-velocity streak, and they also burst intermittently. An example is given in Figure 6.11(a), which displays the time evolution of the Reynolds stress,  $-\langle uv \rangle$ , averaged over wall-parallel planes, as a function of the wall distance. The top panel of the Figure reveals that the stress-producing events are temporally intermittent. The averaging can be separated into points in which the velocity perturbations are in the different quadrants of the  $(u, v)$  plane. The two lower panels of Figure 6.11(a) display the time history of the average stress for points in the two main stress-producing quadrants. It is not surprising that ejections,  $(u < 0, v > 0)$ , move away from the wall, while sweeps,  $(u > 0, v < 0)$ , move towards it, but it is interesting that the vertical velocities are similar in both cases (of the order of  $u_\tau$ ), and remarkably uniform over the region depicted, suggesting that the two events are parts of some common larger structure.

The evolution of the velocity field during the burst is shown in Figure 6.11(b), and looks remarkably similar to the events in the buffer layer. The single streak in the simulation box becomes increasingly wavy, and is eventually destroyed by the instability, but it should be emphasized that, in spite of the obvious similarities between Figures 6.11(b) and 6.5(b), the boxes in Figure 6.11(b) are about fifteen times wider than those in the buffer layer, and that the streak is now a fully turbulent multiscale object. The bursting period can be estimated from the temporal evolution of different integrated quantities, and depends on the distance to the wall ( $u_\tau T \approx 6y$ ), rather than on the size of box. Wider boxes simply continue the linear trend farther from the wall. As in the buffer layer, we know less about the temporal evolution of the structures in full-size flows, but the temporal variability of the statistics of the minimal boxes is essentially identical to the variability among randomly chosen sub-boxes of the same size in full channels, suggesting that the processes are similar in the full and restricted systems (for details, see Flores and Jiménez, 2010).

On the other hand, it is also unlikely in this case that the minimal boxes represent the complete behaviour of real flows. In a hypothetical cycle in which the instabilities of the large-scale low-velocity cones create the intermittent ejections associated with the vortex tangles, which in turn create new streaks, the minimal boxes can probably only represent correctly the part connected with a single instability event. For example, the formation of the composite streak in Figure 6.9(d) clearly requires more space than the minimal dimensions, and the processes responsible for the concatenation of these subunits into larger wholes, especially regarding their apparent alignment into streamwise streaks, are not understood.

This qualitative model does not include interactions among different wall distances. Each streak instability creates an ejection of comparable size, which in turn recreates a commensurate streak. The fact that small boxes sustain healthy turbulence up to a certain wall distance without the corresponding larger scales suggests that the overlying structures are unnecessary for the smaller ones. Numerical experiments in which the viscous wall cycle is artificially removed, but whose outer-flow ejections and streaks remain essentially identical to those above smooth walls (Flores and Jiménez, 2006; Flores et al., 2007), suggest that the small-scale structures below a given ejection are also essentially accidental. Experimentally, this is equivalent to the classical observation that the outer parts of turbulent boundary layers are independent of wall roughness (Townsend, 1976; Jiménez, 2004). Note, however, that this independence among scales cannot be complete, because the central constraint of wall-bounded turbulence is that the mean momentum transfer has to be balanced among the different wall distances. That is what fixes the relative intensity of the momentum-carrying structures of different sizes.

It is not difficult to construct conceptual feed-back models in which locally weak structures, with too little Reynolds stress, result in the local acceleration of the mean velocity profile, which in turn leads to local enhancements of the velocity gradient and to the strengthening of the local fluctuations. But one should beware of two-scale models of turbulence, which in this case would be one scale of fluctuations and the mean flow. Everything that we know about turbulence points to its multiscale character, without privileged spectral gaps. It is more likely that any interaction leading to the adjustment of the intensities of the structures at different wall distances takes place between structures of roughly similar sizes, without necessarily passing through the mean flow. Elucidating such a mechanism will require either fairly large Reynolds numbers, or clever postprocessing techniques.

The models outlined in this section have been mostly derived from computational experiments. The experimental observations of the past decade have suggested a different scenario in which the basic object is a hairpin vortex growing from the wall, whose induced velocity creates the low momentum ramps mentioned above (Adrian et al., 2000). The hairpins regenerate each other, creating packets that are responsible for the long observed streaks (Christensen and Adrian, 2001).

Some of the differences between the two models are probably notational. For example, individual hairpins can be made to correspond to the instabilities of the shear layers around the streaks, especially if hairpins are allowed to be irregular or incomplete. The formation of vortex packets would corre-

spond to the lengthening of the streaks in the wake of the bursts. Similarly, the respective emphases on vortices and on larger eddies might be influenced by the relatively coarse resolution of most experiments, which are unable to resolve individual vortices. Relying on conditional averages, as in Figure 6.9(b), or on limited statistics based on selected ‘recognizable’ objects, might give an impression of symmetry that does not apply to more typical individual structures. But it is harder to reconcile the respective treatments of the importance of the wall. The ‘numerical’ model emphasizes the effect of the local velocity shear, while the ‘experimental’ one appears to require the formation of hairpins at, or near, the buffer region. We have argued above that the evidence supports the former, but the experimental observations are also plausible. The theoretical results are ambiguous. The original simulations supporting the growth of hairpin packets were carried out by Zhou et al. (1999) on a laminar flow with a mean turbulent velocity profile, using molecular viscosity. They show hairpins growing away from the wall. But Flores and Jiménez (2005) have argued that large structures feel the effect of small-scale turbulent dissipation, and should be studied using some kind of subgrid eddy viscosity. When that is done, vorticity rises very little before it is dissipated.

Only recently has it become possible to compile flow animations fully resolved in both space and time (Lozano-Durán and Jiménez, 2010), and their analysis has only just begun. The resolution of the controversy about the flow of causality in the logarithmic layer will have to wait for those results.

### 6.5 Coherent structures and dynamical systems

We have seen in the previous sections several instances in which the behaviour of the flow can be qualitatively explained in terms of deterministic interactions among structures. In fact, although apparently infinite-dimensional, the turbulent motion of a viscous fluid in a finite domain, governed by the Navier–Stokes equations, i.e., by partial differential evolution equations is a finite-dimensional dynamical system. Physically, the reason is that small-scale motions are smoothed by viscosity.

There is a mathematical proof of the existence of approximate inertial manifolds for the Navier–Stokes equations and this proof leads to an approximate relation between the dominant modes and the higher-order ones that can be truncated (Foias et al., 2001). Within such a manifold, the Navier–Stokes equations can be approximated by a finite-dimensional system of ordinary differential evolution equations. For example, Keefe et al.

(1992) demonstrated numerically that a spatially periodic turbulent channel flow with  $\delta^+ = 80$ , simulated with a spatial resolution of  $16 \times 33 \times 16$ , was really confined to a finite-dimensional strange attractor whose Kaplan–Yorke dimension was estimated to be 780, about 10% of the total number of numerical degrees of freedom. That measure of the dimension of the attractor is based on the Lyapunov exponents of the system, and approximately measures the dimension of the subspace whose volume neither increases nor decreases during the evolution of the flow (Frederickson et al., 1983).

Dynamical-system theory tells us that coherent structures in turbulent flows may be thought of as low-dimensional invariant sets in phase space, in the neighbourhood of which the system spends a substantial fraction of time, as suggested in Jiménez (1987). Spatio-temporally organized structures appear when a turbulent state approaches such an invariant set. Possible invariant solutions are simple saddles in phase space, such as steady travelling waves, or orbits that are periodic in time in some moving frame of reference. It is known that the statistical properties of chaotic low-dimensional dynamical systems can be estimated from the coherent states represented by unstable periodic orbits (Cvitanović, 1987; Artuso et al., 1990a,b; Christiansen et al., 1997). In this section, we will restrict ourselves to such relatively simple solutions, even if coherent structures can also correspond to more complex sets in much lower dimensional systems, such as the strange attractors of some highly reduced dynamical systems obtained from the Navier–Stokes equations by proper orthogonal decomposition (see Holmes et al., 1996).

The computation of such solutions in ideal, infinitely large, plane channels, or in experimental rectangular ducts with inflow and outflow boundary conditions, is at the moment beyond our computational capabilities, but we have argued above that the purpose of theory is not necessarily to reproduce experiments, but to give information on how the cases of interest could eventually be predicted. Numerical simulations in doubly periodic domains are known to reproduce well the statistics of experiments, and we have seen that even the minimal flow units invented by Jiménez and Moin (1991) for plane Poiseuille turbulence, and later applied by Hamilton et al. (1995) to plane Couette turbulence, represent well at least part of the buffer layer. Such reduced systems are small enough for their coherent structures to be described in terms of a simple invariant solutions, and we will see below that several have been found for doubly- or singly-periodic ‘minimal’ domains in plane Couette, Poiseuille, Hagen–Poiseuille, and square-duct flows.

The first solutions of this kind were obtained by Nagata (1990) in plane Couette flow. That flow is stable to infinitesimal disturbances at all Reynolds

numbers, so that nonlinear solutions cannot simply be found by continuation from the laminar state. Nagata (1990) found his solution by first imposing a spanwise rotation on the system, which led to a sequential series of bifurcations of two- and three-dimensional steady solutions from the laminar state. He then extended one of those three-dimensional nonlinear solutions to the non-rotating case. Clever and Busse (1992) obtained the same three-dimensional solution by initially imposing a temperature difference between the two horizontal walls of a Couette flow, and the same solution was again found by Waleffe (1998, 2003) who, based on the physical insight previously gained by Hamilton et al. (1995) into the self-sustaining process of turbulent coherent structures, initiated his continuation from an artificial flow with streamwise-independent longitudinal vortices induced by an imposed body force. The three-dimensional equilibrium solution found by those three groups arises from a saddle-node bifurcation at a finite value of the Reynolds number, above which it splits into two solution branches. As we will see later, the solutions of the upper branch contain a wavy low-velocity streak and a pair of staggered counter-rotating streamwise vortices, and are remarkably similar to the coherent structures of the turbulent buffer layer. The solutions in the lower branch are closer to the laminar state. Other equilibrium solutions have been found more recently for Couette flow by Nagata (1997); Schmiegel (1999); Gibson et al. (2008, 2009); Itano and Generalis (2009). They are not necessarily related to the one originally identified by Nagata (1990), but they have been used to discuss coherent structures and the subcritical transition to turbulence.

In contrast to plane Couette flow, laminar plane Poiseuille flow in a channel is unstable to infinitesimal disturbances beyond a certain Reynolds number, from where a two-dimensional equilibrium travelling-wave solution bifurcates subcritically. A three-dimensional solution originating from the two-dimensional wave was found by Ehrenstein and Koch (1991), while Waleffe (1998, 2001, 2003) and Itano and Toh (2001) found families of three-dimensional steady travelling waves that are not known to be connected to the laminar state. In Waleffe (1998, 2001, 2003), he used the artificial-force approach to construct nonlinear steady travelling waves with a reflectional symmetry with respect to the channel central plane, which also contain streaks and vortices. His Poiseuille solution can be continuously connected to the Nagata (1990) solution for plane Couette flow (Waleffe, 2003). Itano and Toh (2001) solution also includes streaks and vortices, but they are localized near one of the two walls. A three-dimensional steady travelling with a very similar structure was found by Jiménez and Simens (2001) in a so-called ‘autonomous’ flow that is confined to the vicinity of one wall under

the action of a damping filter (Jiménez and Pinelli, 1999). That is the case used in Figure 6.3(b) to compare the fluctuation profiles of simple solutions with those of real turbulence.

The laminar Hagen–Poiseuille flow in a circular pipe is also linearly stable at all Reynolds numbers, but Faisst and Eckhardt (2003) and Wedin and Kerswell (2004) have recently discovered three-dimensional steady travelling-wave solutions by using the self-sustaining approach proposed by Waleffe (1998, 2003). Both groups obtain the same solution, which possesses discrete rotational symmetry with respect to the pipe axis, with wavy low-velocity streaks flanked by staggered streamwise vortices. The solution with three-fold rotational symmetry arises from a saddle-node bifurcation at the lowest Reynolds number, although it was later found that travelling waves without any discrete rotational symmetry exist at much lower Reynolds numbers (Pringle and Kerswell, 2007).

As in circular pipes, the laminar flow in a square duct is linearly stable, and no travelling-wave solutions were known until three three-dimensional steady travelling waves were found using the artificial-force approach or internal heating. The two found by Wedin et al. (2009) and Okino et al. (2010) have low- or high-velocity streaks and streamwise vortices on only two opposite walls, while the other two walls of the duct are empty. The one found by Uhlmann et al. (2010), on the other hand, has streaks and vortices on the four walls, so that its streamwise-averaged cross-flow velocity exhibits an eight-vortex pattern closely resembling the mean secondary flow of experimental turbulent ducts (Figure 6.12). This correspondence gives some support to the numerical evidence that the mean secondary motion of low-Reynolds-number square-ducts is a direct consequence of coherent structures (Pinelli et al., 2010).

We already mentioned in §6.3 and §6.4 that turbulent flow is really unsteady, even in small boxes, and that something like a bursting cycle is necessary for regenerating the fluctuations. However, even if we have just seen that three-dimensional equilibrium solutions reproducing buffer-layer coherent structures are available for a variety of wall-bounded flows, only a few periodic solutions have recently been discovered.

In plane Couette flow, Clever and Busse (1997) analysed the linear stability of Nagata (1990) three-dimensional steady solution, and identified a Hopf bifurcation from where a temporally-periodic three-dimensional nonlinear solution arises. They continued that solution within its stable parameter range by forward time integration, but found that its properties did not differ too much from those of the steady solution due to the small amplitude of the oscillations. Using an iterative method to minimize the recurrence

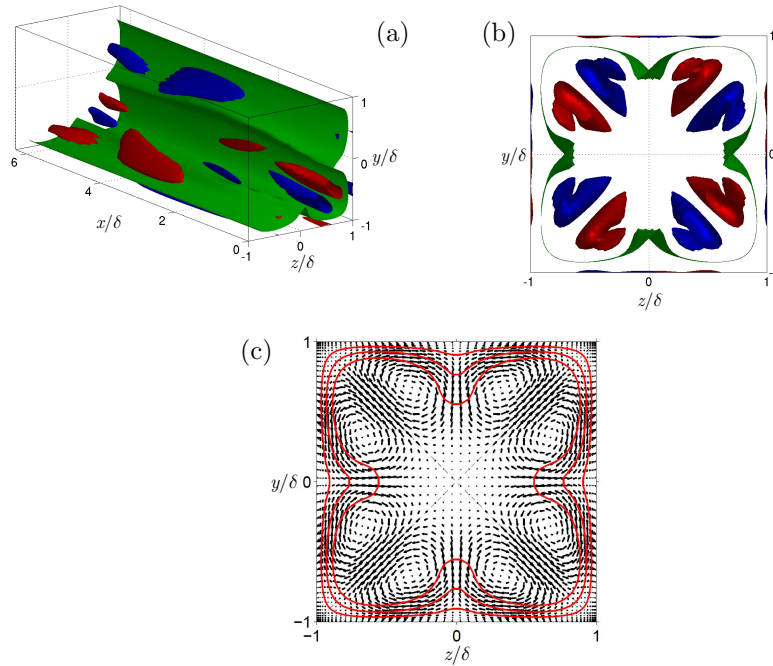


Figure 6.12 Shape of the eight-vortex steady upper-branch travelling wave in a duct, at bulk Reynolds number  $Re = U_b \delta / \nu = 1404$ , and streamwise wavelength  $L_x / \delta = 2\pi$  (Uhlmann et al., 2010). (a, b) The green sheet near the wall is an isosurface of the streamwise velocity, 0.55 times its maximum. The blue and red tubular structures are the streamwise vorticity,  $\pm 0.65$  times its maximum ( $\omega_x^\pm = \pm 0.0655$ ). Figure (a) only shows surfaces to one side of a duct diagonal. (c) The contour lines are isolines of the streamwise-averaged streamwise velocity, (0.25, 0.5, 0.75 times its maximum). The arrows are the streamwise-averaged secondary velocity.

error, Kawahara and Kida (2001) found a more unsteady three-dimensional unstable periodic solution for plane Couette flow, which reproduces much better the full regeneration cycle of near-wall coherent structures, i.e., the formation and development of low-velocity streaks by decaying streamwise vortices, the bending of the streaks followed by the regeneration of the vortices, the breakdown of the streaks, and the rapid development of the vortices. They also obtained a gentler periodic solution that represents a weak spanwise standing-wave motion of the low-velocity streak.

More recently Viswanath (2007) has developed a new method based on Newton–Krylov iteration and on a locally-constrained optimal hook step, and applied it to the computation of periodic solutions in Couette flow. His method is matrix-free, and drastically reduces the computational time and memory required for the Newton iteration. Using it, he obtained five

new three-dimensional periodic solutions that demonstrate the breakup and reorganization of near-wall coherent structures.

In plane Poiseuille flow, Toh and Itano (2003) identified a three-dimensional periodic-like solution that could originate from a heteroclinic connection between two equivalent Itano and Toh (2001) steady travelling waves that differ from each other by a spanwise shift of half a wavelength. Their solution is reminiscent of the heteroclinic cycle identified in a highly reduced dynamical-system approximation to near-wall turbulence by Aubry et al. (1988), who also observed a connection between two fixed points differing by a similar spanwise shift.

More recently, Duguet et al. (2008) found a three-dimensional periodic solution in Hagen–Poiseuille flow that bifurcates from the Pringle and Kerswell (2007) travelling wave without any discrete rotational symmetry.

Most of the unstable periodic orbits have been found for wall bounded shear flows, but there are a few exceptions. One is the periodic solution found by van Veen et al. (2006) in a Kida–Pelz highly-symmetric flow in a triply periodic domain (Kida, 1985), which reproduces the universal Kolmogorov (1941) energy spectrum with the right energy dissipation rate, even though its Reynolds number is too low to identify any real inertial range. Another periodic solution was obtained in the GOY (Gledzer–Ohkitani–Yamada) shell model by Kato and Yamada (2003), who observed that the solution not only exhibits the Kolmogorov inertial-range energy spectrum, but also intermittency.

It is curious that averaging along a single unstable periodic orbit of relatively short period, such as in these solutions or in those mentioned above for plane Couette flow (Kawahara and Kida, 2001; Viswanath, 2007), reproduces so well typical properties of turbulence, such as the energy spectra and the r.m.s. velocity profiles, which are long-time averages along true turbulent orbits. A possible interpretation has recently been proposed by Saiki and Yamada (2009, 2010), who showed that periodic orbits are really special. If one evaluates the statistical mean and variance of the time averages of dynamical variables along distinct periodic orbits with similar periods, the mean is nearly the same as that along chaotic segments with corresponding lengths, but the variance is significantly smaller than along the chaotic segments. This observation suggests that short periodic orbits might be better representations of the statistical behaviour of turbulent systems than comparable segments of their true temporal evolution in the sense that the statistical values along periodic orbits are confined to a narrower range around the exact one.

We now discuss the possible relevance of these simple invariant solutions

to wall-bounded turbulence. All the solutions just described are unstable at the Reynolds numbers at which turbulence is observed, but the dimensions of their unstable manifolds in phase space are typically low (Waleffe, 2001; Kawahara, 2005; Wang et al., 2007; Kerswell and Tutty, 2007; Viswanath, 2009). Therefore, although we should not expect to observe them as such in real turbulence, a generic turbulent solution could approach them and spend a substantial fraction of its lifetime in their neighbourhood. In a nonlinear dynamical system the transverse intersections of the stable and unstable manifolds of the same or different periodic orbits lead to homoclinic or heteroclinic orbits, and to the appearance of chaotic behaviour through Smale's horseshoe (Guckenheimer and Holmes, 1986). Therefore, the tangle of stable and unstable manifolds of the above simple invariant solutions could represent turbulence dynamics, while the simple solutions themselves would represent coherent structures.

To ascertain whether that is really the case for near-wall turbulence, Jiménez et al. (2005) collected the simple solutions available at the time for Poiseuille and Couette flows, some of which we have seen to have velocity fluctuation profiles strongly reminiscent of real turbulence. The characteristics of those profiles are summarized in Figure 6.13, which has been adapted from that paper by adding some of the solutions that have been found since then. Each solution is represented by a single point whose coordinates are the maximum values,  $u'_{\max}$  and  $v'_{\max}$ , of its intensity profiles. Most solutions fall into one of two classes: a 'vortex-dominated' (upper) family, characterized by smaller  $u'_{\max}$  and larger  $v'_{\max}$ , and a 'streak-dominated' (lower) one, characterized by larger  $u'_{\max}$  and smaller  $v'_{\max}$ . As in §6.3 we take the streamwise and wall-normal velocity fluctuations as respectively representing the intensities of the streamwise velocity streaks and of the quasi-streamwise vortices.

In the upper-left corner of Figure 6.13 we find the vortex-dominated solutions, and in the lower-right corner the streak-dominated ones. The former are represented by Kawahara and Kida (2001) dynamic periodic solution, by Nagata (1990) upper-branch steady solutions, and by Jiménez and Simens (2001) autonomous travelling waves. The temporal averages of Viswanath (2007) periodic solutions in plane Couette flow are also part of this family. These are the solutions closer to real turbulence, and the full channel of Kim et al. (1987) is included in the figure as comparison.

The streak-dominated family includes Kawahara and Kida (2001) gentle periodic orbit, Nagata (1990) lower-branch steady solutions, the permanent wave obtained by Itano and Toh (2001) in Poiseuille flow, and the heteroclinic connection identified by Toh and Itano (2003). The figure includes the

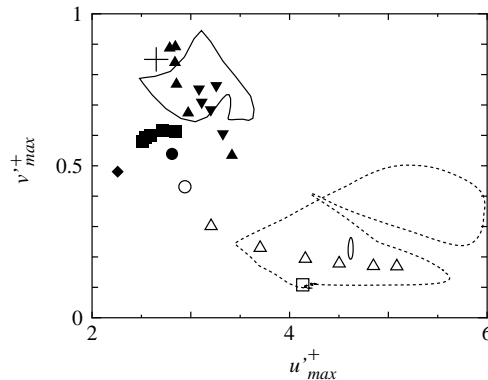


Figure 6.13 Classification into upper and lower families of the simple solutions, in terms of their maximum streamwise and wall-normal r.m.s. velocities,  $u'_{\max}$  and  $v'_{\max}$ . Solid symbols are classified as upper-branch, and open ones as lower-branch. The solid large and small loops represent the dynamic ( $L_x^+ \times L_z^+ \times \delta^+ = 190 \times 130 \times 34$ ) and the gentle ( $L_x^+ \times L_z^+ \times \delta^+ = 154 \times 105 \times 28$ ) periodic solutions at  $Re = 400$  in Kawahara and Kida (2001).  $\triangle$ , Nagata (1990) steady solution for several values of the spanwise wavelength at  $Re = 400$  and  $L_x/\delta = 2\pi$  (upper branch,  $L_z^+ \times \delta^+ = 76 - 132 \times 35$ ; lower branch,  $L_z^+ \times \delta^+ = 53 - 92 \times 24 - 25$ ).  $\blacksquare$ , autonomous solutions in Jiménez and Simens (2001) ( $L_x^+ \times L_z^+ \times \delta_1^+ = 151 - 189 \times 180 \times 38 - 46$ , where  $\delta_1$  is the filter height).  $\bullet$ , Waleffe (2003) upper-branch solution for  $Q/\nu = 1303$ , where  $Q$  is the volume flux per unit span.  $L_x^+ \times L_z^+ \times \delta^+ = 387 \times 149 \times 123$ ;  $\circ$ , Waleffe (2003) lower-branch solution for  $Q/\nu = 1390$ ,  $L_x^+ \times L_z^+ \times \delta^+ = 379 \times 146 \times 121$ ;  $\square$ , Itano and Toh (2001) asymmetric wave for  $Q/\nu = 4000$ ,  $L_x/\delta = \pi$  and  $L_z/\delta = 0.4\pi$ . The dotted loop is the periodic-like solution of Toh and Itano (2003).  $\blacktriangledown$ , temporal averages of Viswanath (2007) periodic solutions (cases  $P_2 - P_6$  in his table 1) for  $Re = 400$  and  $L_x/\delta \times L_z/\delta = 1.75\pi \times 1.2\pi$  in plane Couette flow.  $\blacklozenge$ , upper branch of Uhlmann et al. (2010) eight-vortex travelling-wave solution in square duct flow ( $Re = 1371$ ,  $L_x/\delta = 2\pi$ ). We have also shown the turbulent state computed by Kim et al. (1987) ( $L_x^+ \times L_z^+ \times \delta^+ = 2300 \times 1150 \times 180$ ) by the symbol '+' for comparison.

two permanent waves by Waleffe (2003) for Poiseuille flow, which were classified as lower- or upper-branch in the original reference, but which appear here to be too close to the turning point to differ too much from each other.

The upper-branch of Uhlmann et al. (2010) eight-vortex travelling wave in a square duct is also included, and is relatively close to the upper-family solutions mentioned above, in spite of its significantly different boundary conditions, but the corresponding lower-branch solution has a weaker  $u'_{\max}$  than the upper-branch one, and is thus quite different from the lower-family solutions discussed here.

Besides those statistical differences, the spatial structures of the upper and lower families are also quite different. The two flow fields in Figure 6.14 correspond to the upper and lower Nagata (1990) solutions at comparable Reynolds numbers and dimensions. They differ mainly in the location of the

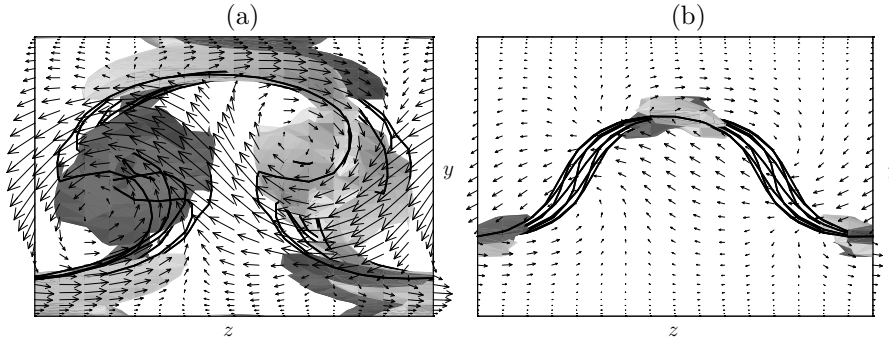


Figure 6.14 Projection of the streamwise vorticity,  $\omega_x$ , and velocity fields in the cross-plane  $(z, y)$ , for (a) the upper-branch ( $L_z^+ = 99$ ), and (b) lower-branch ( $L_z^+ = 67$ ) solutions of Nagata (1990).  $Re = 400$ ,  $L_x/\delta \times L_z/\delta = 2\pi \times 0.9\pi$ . The thick solid lines are different sections of the surface  $u = 0$ , i.e., the critical layer. Arrows are the cross-plane velocities at  $x = 0$ , defined so that the first streamwise harmonic of  $u$  is proportional to  $\cos(2\pi x/L_x)$ . The arrows are uniformly scaled in wall units, and the longest arrows in (a) are roughly  $1.9u_\tau$ . The dark- and light-gray objects are isosurfaces  $\omega_x^\pm = \pm 0.155$ .

streamwise vorticity, which is concentrated in the form of sheets on a critical layer in the case of the lower-branch solution, but which has two concentrated tubular vortices in each flank of the streak in the case of the upper one. The spatial structure of the upper solution reproduces well the near-wall coherent structures, with a pair of counter-rotating staggered streamwise vortices flanking a wavy low-velocity streak (see §6.3). The streamwise vortical structures are responsible for the larger  $v'_{\max}$  in the upper family, but note that there is no one-to-one correspondence between the strength of the vortices and that of the streak. The latter is a consequence of the action of the vortices over a period of time, and this time scale is as important in determining the streak intensity as the vortex strength. There is little doubt that, in the absence of viscosity or of other limiting factor, a long permanent vortex would eventually pump the mean velocity profile into uniform streamwise regions in which the streamwise velocity would be that of one or the other wall. Viscosity or instabilities limit that distortion, and the simplest explanation of the weaker streaks, and smaller  $u'_{\max}$ , of the upper-branch solutions is that the flank vortices shorten the effective time scale of the pumping by providing an effective eddy viscosity that homogenizes the streamwise-velocity profile.

The lower solution family is probably not directly related to turbulence, and it is now believed to play an important role in the subcritical transition to turbulence (Kerswell, 2005; Eckhardt et al., 2007). At Reynolds numbers low enough for laminar flow to be stable, there is a boundary in phase space

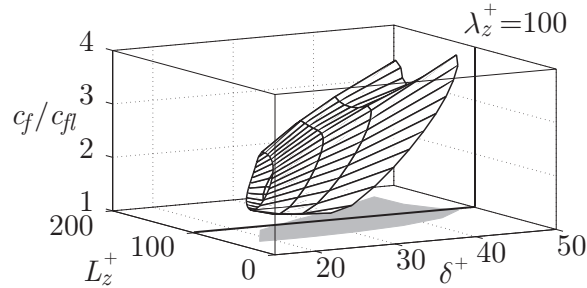


Figure 6.15 Friction coefficient, normalized by a corresponding laminar value,  $c_f/c_{fl}$ , of Nagata (1990) solution for plane Couette flow as a function of the spanwise wavelength  $L_z^+$ , and of the friction Reynolds number  $\delta^+$ . Streamwise wavelength  $L_x/\delta = 2\pi$

that separates the basins of attraction of the turbulent and laminar states. Some of the lower-family solutions for plane Poiseuille and Couette flow have only one unstable direction in phase space, so that those invariant sets and their stable manifolds form the laminar-to-turbulent separatrix (Itano and Toh, 2001; Waleffe, 2003; Kawahara, 2005; Wang et al., 2007; Schneider et al., 2008).

Figure 6.15 shows the friction coefficient of Nagata (1990) solutions normalized with that of the laminar state, for a fixed value of the streamwise wavelength  $L_x/\delta = 2\pi$ , as a function of the spanwise wavelength and of the friction Reynolds number. Both the upper and the lower branches of the solution have higher friction coefficients than the laminar state. The range of spanwise wavelengths for which the solutions exist is always around  $L_z^+ = 100$ , which is close to the observed mean separation of buffer-layer streaks, and the range itself,  $L_z^+ \approx 50 - 150$ , is in good agreement with the range of streak spacings found in experimental turbulent boundary layers by Smith and Metzler (1983),  $\lambda_z^+ \approx 50 - 200$ . The same range of spanwise wavelengths is also found in Kawahara and Kida (2001) stronger periodic solution in plane Couette flow (Kawahara, 2009), and is around the width of the narrowest minimal flow unit for sustained turbulence (Jiménez and Moin, 1991). Although its relation with the above nonlinear states is unclear, linear analysis of the system around the state point corresponding to the averaged turbulent flow demonstrates that a three-dimensional infinitesimal perturbation with  $L_z^+ \approx 100$ , also representing streaks and streamwise vortices, leads to optimal transient growth (del Álamo and Jiménez, 2006).

In pipe flow, on the other hand, Kerswell and Tutty (2007) performed a detailed analysis of the correlations between the velocity fields of a turbulent

state and those of Wedin and Kerswell (2004) travelling waves with discrete rotational symmetry, and showed that turbulence only visits the close vicinity of the travelling waves in phase space for 10% of the time, suggesting that there should be other objects, such as periodic orbits, which turbulence approaches more frequently. More recently, Willis and Kerswell (2008) examined the relation of known travelling-wave solutions with flow states in a long pipe, and suggested that both the lower and upper branches of their solutions sit in an intermediate region of phase space, between laminar and turbulent states, rather than being embedded within the turbulent attractor itself.

We close this section by briefly discussing possible future areas of research in the nascent field of the possible relation between the coherent structures of turbulence and dynamical systems. Although it has turned out that the structures, the dynamics, and the statistics of buffer-layer coherent structures are tantalizingly close to those of some nonlinear equilibria, or to the finite-amplitude oscillations represented by known simple invariant sets in phase space, the dynamical interpretation of the large-amplitude intermittent events observed in the near-wall region remains unclear. One possibility is that those violent events correspond in phase space to the unstable or stable manifolds of the simple invariant solutions just described, or to their connections. Halcrow et al. (2009) have quantitatively identified heteroclinic connections between known equilibrium solutions of plane Couette flow, and van Veen et al. (2011) recently developed a numerical method for computing two-dimensional unstable manifolds in large systems, which they used to significantly extend the unstable manifold of Kawahara and Kida (2001) gentle periodic orbit in plane Couette flow and then to find homoclinic orbits from/to that periodic orbit (van Veen and Kawahara, 2011). These studies are the first steps in the exploration of global phase-space structures in near-wall turbulence.

Another possible research direction relates to the large-scale flow structures of transitional and turbulent wall flows, such as turbulent spots (Dauchoy and Daviaud, 1995), oblique stripes (Prigent et al., 2002), puffs (Wyganski and Champagne, 1973) and large-scale streaks (see §6.4). Most of the available invariant solutions have been obtained in more or less minimal flow units that cannot accommodate those large-scale structures. Spatially localized invariant solutions (including chaotic edge states) in a larger periodic box would be useful for the characterization of transitional large-scale structures (Cherhabili and Ehrenstein, 1997; Ehrenstein et al., 2008; Schneider et al., 2010; Duguet et al., 2009; Willis and Kerswell, 2009; Mellibovsky et al., 2009). We also saw in §6.4 that Flores and Jiménez (2010) have

found quasi-periodic bursts in the logarithmic region of fully turbulent channel flow, strongly reminiscent of the regeneration cycle in the buffer layer, suggesting that the large-scale dynamics in the logarithmic layer might be related to invariant solutions in larger periodic domains.

## 6.6 Conclusions

In summary, our knowledge of wall-bounded turbulence has advanced a lot in the last thirty years, and we have argued that this has been due, in large part, to the availability of reasonably affordable direct numerical simulations. Although we have shown several instances of how that has happened in detail, it may be appropriate to summarize here the nature of the changes that simulations have brought to the study of turbulence.

Every science passes through several stages in its development. The most primitive one is characterized by the scarcity of suitable data, which leads to the appearance of theories attempting to explain the few data available, but whose further predictions cannot be easily tested. Planetary science was a typical example until the advent of space exploration, and turbulence spent much of the XXth century in this stage. Fluid flow is difficult to measure and to visualize, and the available data were relatively few and incomplete. It was possible to propose almost any theory about turbulence structure and dynamics, with relatively few constraints from observations.

The situation began to change in the 1950's with the advent of hot wires, which gave the first glimpses of the structure of the turbulent eddies, and it became a flood with direct numerical simulations. In the same way that it became impossible to speak about canals in Mars after the first space probes, the data generated by DNS, and to a lesser but important extent by experimental visualisations and PIV, have produced much tighter limits for our theories.

It is probably true that the data required to test almost any theory about the dynamics of canonical turbulent flows already exist in some numerical data base, or that, if it were known which data are missing, they could probably be easily computed in a relatively short time.

What this new development denies us is the freedom to speculate. Almost anything that can be proposed can be tested, and the nature of the turbulence problem is quickly changing from one of accumulating new data to one of interpreting existing ones. It is not necessarily a simpler problem, but it is different from much of what we have been doing up to now. The consequences for turbulence theory can only be guessed at this moment.

**Acknowledgments** The preparation of this article has been supported in part by the Spanish CICYT, under grant TRA2009-11498, by the European Research Council Advanced Grant ERC-2010.AdG-20100224, and a Grant-in-Aid for Scientific Research (B) from the Japanese Society for the Promotion of Science. The authors cordially thank D. Viswanath and M. Uhlmann for the original data of periodic solutions in Couette flow, and of travelling waves in a square-duct, and O. Flores for Figures 6.9(a) and 6.9(c).

### References

- Abe, H., Kawamura, H., and Matsuo, Y. 2004. Surface heat-flux fluctuations in a turbulent channel flow up to  $Re_\tau = 1020$  with  $Pr = 0.025$  and  $0.71$ . *Int. J. Heat Fluid Flow*, **25**, 404–419.
- Adrian, R. J. 2007. Hairpin vortex organization in wall turbulence. *Phys. Fluids.*, **19**, 041301.
- Adrian, R. J., Meinhart, C. D., and Tomkins, C. D. 2000. Vortex organization in the outer region of the turbulent boundary layer. *J. Fluid Mech.*, **422**, 1–54.
- Afzal, N., and Yajnik, K. 1973. Analysis of turbulent pipe and channel flows at moderately large Reynolds number. *J. Fluid Mech.*, **61**, 23–31.
- Artuso, R., Aurell, E., and Cvitanović, P. 1990a. Recycling of strange sets: I. Cycle expansions. *Nonlinearity*, **3**, 325–359.
- Artuso, R., Aurell, E., and Cvitanović, P. 1990b. Recycling of strange sets: II. Applications. *Nonlinearity*, **3**, 361–386.
- Aubry, N., Holmes, P., Lumley, J. L., and Stone, E. 1988. The dynamics of coherent structures in the wall region of a turbulent boundary layer. *J. Fluid Mech.*, **192**, 115–173.
- Bakewell, H. P., and Lumley, J. L. 1967. Viscous sublayer and adjacent wall region in turbulent pipe flow. *Phys. Fluids*, **10**, 1880–1889.
- Barenblatt, G. I., Chorin, A. J., and Prostokishin, V. M. 2000. Self-similar intermediate structures in turbulent boundary layers at large Reynolds numbers. *J. Fluid Mech.*, **410**, 263–283.
- Bradshaw, P. 1967. Inactive motions and pressure fluctuations in turbulent boundary layers. *J. Fluid Mech.*, **30**, 241–258.
- Brown, G. L., and Roshko, A. 1974. On the density effects and large structure in turbulent mixing layers. *J. Fluid Mech.*, **64**, 775–816.
- Butler, K. M., and Farrell, B. F. 1993. Optimal perturbations and streak spacing in wall-bounded shear flow. *Phys. Fluids A*, **5**, 774–777.
- Cherhabili, A., and Ehrenstein, U. 1997. Finite-amplitude equilibrium states in plane Couette flow. *J. Fluid Mech.*, **342**, 159–177.
- Christensen, K. T., and Adrian, R. J. 2001. Statistical evidence of hairpin vortex packets in wall turbulence. *J. Fluid Mech.*, **431**, 433–443.
- Christiansen, F., Cvitanović, P., and Putkaradze, V. 1997. Spatiotemporal chaos in terms of unstable recurrent patterns. *Nonlinearity*, **10**, 55–70.

- Clever, R. M., and Busse, F. H. 1992. Three-dimensional convection in a horizontal fluid layer subjected to a constant shear. *J. Fluid Mech.*, **234**, 511–527.
- Clever, R. M., and Busse, F. H. 1997. Tertiary and quaternary solutions for plane Couette flow. *J. Fluid Mech.*, **344**, 137–153.
- Cvitanović. 1987. Invariant measurement of strange sets in terms of cycles. *Phys. Rev. Lett.*, **61**, 2729–2732.
- Darcy, H. 1854. Recherches expérimentales relatives au mouvement de l'eau dans les tuyaux. *Mém. Savants Etrang. Acad. Sci. Paris*, **17**, 1–268.
- Dauchot, O., and Daviaud, F. 1995. Finite amplitude perturbation and spots growth mechanism in plane Couette flow. *Phys. Fluids*, **7**, 335–343.
- Deardorff, J. W. 1970. A numerical study of three-dimensional turbulent channel flow at large Reynolds number. *J. Fluid Mech.*, **41**, 453–480.
- Deardorff, J. W. 1973. The use of subgrid transport equations in a three-dimensional model of atmospheric turbulence. *J. Fluid Eng.*, **95**, 429–438.
- deGraaff, D. B., and Eaton, J. K. 2000. Reynolds number scaling of the flat-plate turbulent boundary layer. *J. Fluid Mech.*, **422**, 319–346.
- del Álamo, J. C., and Jiménez, J. 2003. Spectra of very large anisotropic scales in turbulent channels. *Phys. Fluids*, **15**, L41–L44.
- del Álamo, J. C., and Jiménez, J. 2006. Linear energy amplification in turbulent channels. *J. Fluid Mech.*, **559**, 205–213.
- del Álamo, J. C., Jiménez, J., Zandonade, P., and Moser, R. D. 2004. Scaling of the energy spectra of turbulent channels. *J. Fluid Mech.*, **500**, 135–144.
- del Álamo, J. C., Jiménez, J., Zandonade, P., and Moser, R. D. 2006. Self-similar vortex clusters in the logarithmic region. *J. Fluid Mech.*, **561**, 329–358.
- Duguet, Y., Pringle, C. C., and Kerswell, R. R. 2008. Relative periodic orbits in transitional pipe flow. *Phys. Fluids*, **20**, 114102.
- Duguet, Y., Schlatter, P., and Henningson, D. S. 2009. Localized edge states in plane Couette flow. *Phys. Fluids*, **21**, 111701.
- Eckhardt, B., Scheider, T. M., Hof, B., and Westerweel, J. 2007. Turbulence transition in pipe flow. *Ann. Rev. Fluid Mech.*, **39**, 447–468.
- Ehrenstein, U., and Koch, W. 1991. Three-dimensional wavelike equilibrium states in plane Poiseuille flow. *J. Fluid Mech.*, **228**, 111–148.
- Ehrenstein, U., Nagata, M., and Rincon, F. 2008. Two-dimensional nonlinear plane Poiseuille–Couette flow homotopy revisited. *Phys. Fluids*, **20**, 064103.
- Faisst, H., and Eckhardt, B. 2003. Traveling waves in pipe flow. *Phys. Rev. Lett.*, **91**, 224502.
- Feller, W. 1971. *An Introduction to Probability theory and its Applications*. third edn. Vol. 1. Wiley. pg. 446–448.
- Flores, O., and Jiménez, J. 2005. Linear dynamics of turbulent structures in the log layer. Pages LR–1 of: *Proc. Div. Fluid Dyn.* Am. Phys. Soc.
- Flores, O., and Jiménez, J. 2006. Effect of wall-boundary disturbances on turbulent channel flows. *J. Fluid Mech.*, **566**, 357–376.
- Flores, O., and Jiménez, J. 2010. Hierarchy of minimal flow units in the logarithmic layer. *Phys. Fluids*, **22**, 071704.

- Flores, O., Jiménez, J., and del Álamo, J. C. 2007. Vorticity organization in the outer layer of turbulent channels with disturbed walls. *J. Fluid Mech.*, **591**, 145–154.
- Foias, C., Manley, O., Rosa, R., and Temam, R. 2001. *Navier–Stokes Equations and Turbulence*. Cambridge University Press.
- Frederickson, P., Kaplan, J. L., Yorke, E. D., and Yorke, J. A. 1983. The Lyapunov dimension of strange attractors. *J. Diff. Equat.*, **49**, 185–207.
- Gaster, M., Kit, E., and Wygnanski, I. 1985. Large-scale structures in a forced turbulent mixing layer. *J. Fluid Mech.*, **150**, 23–39.
- Gibson, J. F., Halcrow, J., and Cvitanović, P. 2008. Visualizing the geometry of state space in plane Couette flow. *J. Fluid Mech.*, **611**, 107–130.
- Gibson, J. F., Halcrow, J., and Cvitanović, P. 2009. Equilibrium and travelling-wave solutions of plane Couette flow. *J. Fluid Mech.*, **638**, 243–266.
- Guckenheimer, J., and Holmes, P. 1986. *Nonlinear Oscillations, Dynamical Systems, and Bifurcations of Vector Fields*, 2nd ed. Springer Verlag.
- Hagen, G. H. L. 1839. Über den Bewegung des Wassers in engen cylindrischen Röhren. *Poggendorfs Ann. Physik Chemie*, **46**, 423–442.
- Halcrow, J., Gibson, J. F., and Cvitanović, P. 2009. Heteroclinic connections in plane Couette flow. *J. Fluid Mech.*, **621**, 365–376.
- Hamilton, J. M., Kim, J., and Waleffe, F. 1995. Regeneration mechanisms of near-wall turbulence structures. *J. Fluid Mech.*, **287**, 317–348.
- Ho, C. H., and Huerre, P. 1984. Perturbed free shear layers. *Ann. Rev. Fluid Mech.*, **16**, 365–424.
- Holmes, P., Lumley, J. L., and Berkooz, G. 1996. *Turbulence, Coherent Structures, Dynamical Systems and Symmetry*, 1st ed. Cambridge University Press.
- Hoyas, S., and Jiménez, J. 2006. Scaling of the velocity fluctuations in turbulent channels up to  $Re_\tau = 2003$ . *Phys. Fluids*, **18**, 011702.
- Hoyas, S., and Jiménez, J. 2008. Reynolds number effects on the Reynolds-stress budgets in turbulent channels. *Phys. Fluids*, **20**, 101511.
- Hutchins, N., and Marusic, I. 2007. Evidence of very long meandering features in the logarithmic region of turbulent boundary layers. *J. Fluid Mech.*, **579**, 467–477.
- Itano, T., and Generalis, S. C. 2009. Hairpin vortex solution in planar Couette flow: A tapestry of knotted vortices. *Phys. Rev. Lett.*, **102**, 114501.
- Itano, T., and Toh, S. 2001. The dynamics of bursting process in wall turbulence. *J. Phys. Soc. Jpn.*, **70**, 703–716.
- Jiménez, J. 1987. Coherent structures and dynamical systems. Pages 323–324 of: *Proc. CTR Summer Program 1987*. Stanford University.
- Jiménez, J. 1998. The largest scales of turbulence. Pages 137–154 of: *CTR Ann. Res. Briefs*. Stanford University.
- Jiménez, J. 2003. Computing high-Reynolds number flows: Will simulations ever substitute experiments? *J. of Turbulence*, **22**.
- Jiménez, J. 2004. Turbulent flows over rough walls. *Ann. Rev. Fluid Mech.*, **36**, 173–196.
- Jiménez, J. 2007. Recent developments in wall-bounded turbulence. *Rev. R. Acad. Cien. Serie A, Mat.*, **101**, 187–203.

- Jiménez, J. 2012. Cascades in wall-bounded turbulence. *Ann. Rev. Fluid Mech.*, **44**, 27–45.
- Jiménez, J., and Hoyas, S. 2008. Turbulent fluctuations above the buffer layer of wall-bounded flows. *J. Fluid Mech.*, **611**, 215–236.
- Jiménez, J., and Moin, P. 1991. The minimal flow unit in near-wall turbulence. *J. Fluid Mech.*, **225**, 221–240.
- Jiménez, J., and Moser, R. D. 2007. What are we learning from simulating wall turbulence? *Phil. Trans. Roy. Soc. A*, **365**, 715–732.
- Jiménez, J., and Pinelli, A. 1999. The autonomous cycle of near wall turbulence. *J. Fluid Mech.*, **389**, 335–359.
- Jiménez, J., and Simens, M. P. 2001. Low-dimensional dynamics in a turbulent wall flow. *J. Fluid Mech.*, **435**, 81–91.
- Jiménez, J., Wray, A. A., Saffman, P. G., and Rogallo, R. S. 1993. The structure of intense vorticity in isotropic turbulence. *J. Fluid Mech.*, **255**, 65–90.
- Jiménez, J., del Álamo, J. C., and Flores, O. 2004. The large-scale dynamics of near-wall turbulence. *J. Fluid Mech.*, **505**, 179–199.
- Jiménez, J., Kawahara, G., Simens, M. P., Nagata, M., and Shiba, M. 2005. Characterization of near-wall turbulence in terms of equilibrium and ‘bursting’ solutions. *Phys. Fluids*, **17**, 015105.
- Kato, S., and Yamada, M. 2003. Unstable periodic solutions embedded in a shell model turbulence. *Phys. Rev. E*, **68**, 025302(R).
- Kawahara, G. 2005. Laminarization of minimal plane Couette flow: Going beyond the basin of attraction of turbulence. *Phys. Fluids*, **17**, 041702.
- Kawahara, G. 2009. Theoretical interpretation of coherent structures in near-wall turbulence. *Fluid Dynamics Research*, **41**, 064001.
- Kawahara, G., and Kida, S. 2001. Periodic motion embedded in plane Couette turbulence: regeneration cycle and burst. *J. Fluid Mech.*, **449**, 291–300.
- Kawahara, G., Jiménez, J., Uhlmann, M., and Pinelli, A. 2003. Linear instability of a corrugated vortex sheet – a model for streak instability. *J. Fluid Mech.*, **483**, 315–342.
- Keefe, L., Moin, P., and Kim, J. 1992. The dimension of attractors underlying periodic turbulent Poiseuille flow. *J. Fluid Mech.*, **242**, 1–29.
- Kerswell, R. R. 2005. Recent progress in understanding the transition to turbulence in a pipe. *Nonlinearity*, **18**, R17–R44.
- Kerswell, R. R., and Tutty, O. R. 2007. Recurrence of travelling waves in transitional pipe flow. *J. Fluid Mech.*, **584**, 69–102.
- Kida, S. 1985. Three-dimensional periodic flows with high-symmetry. *J. Phys. Soc. Japan*, **54**, 3132–2136.
- Kim, J. 1985. Turbulence structures associated with the bursting event. *Phys. Fluids*, **28**, 52–58.
- Kim, J., and Hussain, F. 1993. Propagation velocity of perturbations in channel flow. *Phys. Fluids A*, **5**, 695–706.
- Kim, J., Moin, P., and Moser, R. D. 1987. Turbulence statistics in fully developed channel flow at low Reynolds number. *J. Fluid Mech.*, **177**, 133–166.
- Kim, K.C., and Adrian, R. J. 1999. Very large-scale motion in the outer layer. *Phys. Fluids*, **11**, 417–422.

- Kline, S. J., Reynolds, W. C., Schraub, F. A., and Runstadler, P. W. 1967. Structure of turbulent boundary layers. *J. Fluid Mech.*, **30**, 741–773.
- Kolmogorov, A. N. 1941. The local structure of turbulence in incompressible viscous fluids at very large Reynolds numbers. *Dokl. Akad. Nauk. SSSR*, **30**, 301–305. Reprinted in *Proc. Roy. Soc. London. A* **434**, 9–13 (1991).
- Lee, S.-H., and Sung, H. J. 2007. Direct numerical simulation of the turbulent boundary layer over a rod-roughened wall. *J. Fluid Mech.*, **584**, 125–146.
- Lee, S.-H., and Sung, H. J. 2011. Very-large-scale motions in a turbulent boundary layer. *J. Fluid Mech.*, **673**, 80–120.
- Lozano-Durán, A., and Jiménez, J. 2010. Time-resolved evolution of the wall-bounded vorticity cascade. Pages EB–3 of: *Proc. Div. Fluid Dyn.* Am. Phys. Soc.
- Marusic, I., and Adrian, R. J. 2012. The eddies and scales of wall-turbulence. *This volume*.
- Mathis, R., Hutchins, N., and Marusic, I. 2009. Large-scale amplitude modulation of the small-scale structures in turbulent boundary layers. *J. Fluid Mech.*, **628**, 311–337.
- Meinhart, C. D., and Adrian, R. J. 1995. On the existence of uniform momentum zones in a turbulent boundary layer. *Phys. Fluids*, **7**, 694–696.
- Mellibovsky, F., Meseguer, A., Schneider, T. M., and Eckhardt, B. 2009. Transition in localized pipe flow turbulence. *Phys. Rev. Lett.*, **103**, 054502.
- Moin, P., and Kim, J. 1982. Numerical investigation of turbulent channel flow. *J. Fluid Mech.*, **118**, 341–377.
- Moin, P., and Mahesh, K. 1998. Direct numerical simulation: A tool in turbulence research. *Ann. Rev. Fluid Mech.*, **30**, 539–578.
- Moin, P., and Moser, R. D. 1989. Characteristic-eddy decomposition of turbulence in a channel. *J. Fluid Mech.*, **200**, 471–509.
- Morrison, W. R. B., Bullock, K. J., and Kronauer, R. E. 1971. Experimental evidence of waves in the sublayer. *J. Fluid Mech.*, **47**, 639–656.
- Nagata, M. 1990. Three-dimensional finite-amplitude solutions in plane Couette flow: Bifurcation from infinity. *J. Fluid Mech.*, **217**, 519–527.
- Nagata, M. 1997. Three-dimensional traveling-wave solutions in plane Couette flow. *Phys. Rev. E*, **55**, 2023–2025.
- Oberlack, M. 2001. A unified approach for symmetries in plane parallel turbulent shear flows. *J. Fluid Mech.*, **427**, 299–328.
- Obukhov, A. M. 1941. On the distribution of energy in the spectrum of turbulent flow. *Dokl. Akad. Nauk. SSSR*, **32**, 22–24.
- Okino, S., Nagata, M., Wedin, H., and Bottaro, A. 2010. A new nonlinear vortex state in square-duct flow. *J. Fluid Mech.*, **657**, 413–429.
- Österlund, J. M., Johansson, A. V., Nagib, H. M., and Hites, M. 2000. A note on the overlap region in turbulent boundary layers. *Phys. Fluids*, **12**, 1–4.
- Pinelli, A., Uhlmann, M., Sekimoto, A., and Kawahara, G. 2010. Reynolds number dependence of mean flow structure in square duct turbulence. *J. Fluid Mech.*, **644**, 107–122.

- Prigent, A., Grégoire, G., Chaté, H., Dauchot, O., and van Saarloos, W. 2002. Large-scale finite-wavelength modulation within turbulent shear flows. *Phys. Rev. Lett.*, **89**, 014501.
- Pringle, C. C., and Kerswell, R. R. 2007. Asymmetric, helical, and mirror-symmetric traveling waves in pipe flow. *Phys. Rev. Lett.*, **99**, 074502.
- Reddy, S. C., Schmid, P. J., Baggett, J. S., and Henningson, D. S. 1998. On stability of streamwise streaks and transition thresholds in plane channel flows. *J. Fluid Mech.*, **365**, 269–303.
- Reynolds, O. 1894. On the dynamical theory of incompressible viscous fluids and the determination of the criterion. *Phil. Trans. Roy. Soc. London*, **186**, 123–164. Papers, ii, 535.
- Richardson, L. F. 1920. The supply of energy from and to atmospheric eddies. *Proc. Roy. Soc. A*, **97**, 354–373.
- Rogallo, R. S. 1981. *Numerical experiments in homogeneous turbulence*. Tech. Memo 81315. NASA.
- Rogallo, R. S., and Moin, P. 1984. Numerical simulations of turbulent flows. *Ann. Rev. Fluid Mech.*, **16**, 99–137.
- Saiki, Y., and Yamada, M. 2009. Time-averaged properties of unstable periodic orbits and chaotic orbits in ordinary differential equation systems. *Phys. Rev. E*, **79**, 015201(R).
- Saiki, Y., and Yamada, M. 2010. Unstable periodic orbits embedded in a continuous time dynamical system – time averaged properties. *RIMS Kokyuroku*, **1713**, 111–123.
- Schlatter, P., and Örlü, R. 2010. Assessment of direct numerical simulation data of turbulent boundary layers. *J. Fluid Mech.*, **659**, 116–126.
- Schlatter, P., Örlü, R., Li, Q., Fransson, J.H.M., Johansson, A.V., Alfredsson, P. H., and Henningson, D. S. 2009. Turbulent boundary layers up to  $Re_\theta = 2500$  through simulation and experiments. *Phys. Fluids*, **21**, 05702.
- Schmiegel, A. 1999. *Transition to turbulence in linearly stable shear flows*. Ph.D. thesis, Faculty of Physics, Philipps-Universität Marburg.
- Schneider, T. M., Gibson, J. F., Lagha, M., De Lillo, F., and Eckhardt, B. 2008. Laminar-turbulent boundary in plane Couette flow. *Phys. Rev. E*, **78**, 037301.
- Schneider, T. M., Gibson, J. F., and Burke, J. 2010. Snakes and ladders: localized solutions of plane Couette flow. *Phys. Rev. Lett.*, **104**, 104501.
- Schoppa, W., and Hussain, F. 2002. Coherent structure generation in near-wall turbulence. *J. Fluid Mech.*, **453**, 57–108.
- She, Z.-S. 1993. Constrained Euler system for Navier–Stokes turbulence. *Phys. Rev. Lett.*, **70**, 1255–1258.
- Siebesma, A. P., Bretherton, C. S., Brown, A., A.Chlond, Cuxart, J., Duynkerke, P. G., Jiang, H. L., Khairoutdinov, M., Lewellen, D., Moeng, C. H., Sanchez, E., Stevens, B., and Stevens, D. E. 2003. A large eddy simulation intercomparison study of shallow cumulus convection. *J. Atmos. Sci.*, **60**, 1201–1219.
- Siggia, E. D. 1981. Numerical study of small scale intermittency in three-dimensional turbulence. *J. Fluid Mech.*, **107**, 375–406.

- Sillero, J. A., Borrell, G., Gungor, A. G., Jiménez, J., Moser, R.D., and Oliver, T. A. 2010. Direct simulation of the zero-pressure-gradient boundary layer up to  $Re_\theta = 6000$ . Pages EB–4 of: *Proc. Div. Fluid Dyn.* Am. Phys. Soc.
- Simens, M.P., Jiménez, J., Hoyas, S., and Mizuno, Y. 2009. A high-resolution code for turbulent boundary layers. *J. Comput. Phys.*, **228**, 4218–4231.
- Smith, C. R., and Metzler, S. P. 1983. The characteristics of low speed streaks in the near wall region of a turbulent boundary layer. *J. Fluid Mech.*, **129**, 27–54.
- Spalart, P. R., Coleman, G. N., and Johnstone, R. 2008. Direct numerical simulation of the Ekman layer: A step in Reynolds number, and cautious support for a log law with a shifted origin. *Phys. Fluids*, **20**, 101507.
- Swearingen, J. D., and Blackwelder, R. F. 1987. The growth and breakdown of streamwise vortices in the presence of a wall. *J. Fluid Mech.*, **182**, 255–290.
- Tennekes, H., and Lumley, J. L. 1972. *A First Course in Turbulence*. MIT Press.
- Toh, S., and Itano, T. 2003. A periodic-like solution in channel flow. *J. Fluid Mech.*, **481**, 67–76.
- Toh, S., and Itano, T. 2005. Interaction between a large-scale structure and near-wall structures in channel flow. *J. Fluid Mech.*, **524**, 249–262.
- Townsend, A. A. 1961. Equilibrium layers and wall turbulence. *J. Fluid Mech.*, **11**, 97–120.
- Townsend, A. A. 1976. *The Structure of Turbulent Shear Flow*, 2nd ed. Cambridge University Press.
- Uhlmann, M., Kawahara, G., and Pinelli, A. 2010. Traveling-waves consistent with turbulence-driven secondary flow in a square duct. *Phys. Fluid*, **22**, 084102.
- van Veen, L., and Kawahara, G. 2011. Homoclinic tangle on the edge of shear turbulence. *Phys. Rev. Lett.*, **107**, 114501.
- van Veen, L., Kawahara, G., and Matsumura, A. 2011. On matrix-free computation of 2D unstable manifolds. *SIAM J. Sci. Comp.*, **33**, 25–44.
- van Veen, L., Kida, S., and Kawahara, G. 2006. Periodic motion representing isotropic turbulence. *Fluid Dynamics Research*, **38**, 19–46.
- Vincent, A., and Meneguzzi, M. 1991. The spatial structure and statistical properties of homogeneous turbulence. *J. Fluid Mech.*, **225**, 1–25.
- Viswanath, D. 2007. Recurrent motions within plane Couette turbulence. *J. Fluid Mech.*, **580**, 339–358.
- Viswanath, D. 2009. The critical layer in pipe flow at high Reynolds number. *Phil. Trans. Roy. Soc. A*, **367**, 561–576.
- Waleffe, F. 1997. On a self-sustaining process in shear flows. *Phys. Fluids*, **9**, 883–900.
- Waleffe, F. 1998. Three-dimensional coherent states in plane shear flows. *Phys. Rev. Lett.*, **81**, 4140–4143.
- Waleffe, F. 2001. Exact coherent structures in channel flow. *J. Fluid Mech.*, **435**, 93–102.
- Waleffe, F. 2003. Homotopy of exact coherent structures in plane shear flows. *Phys. Fluids*, **15**, 1517–1534.
- Wang, J., Gibson, J., and Waleffe, F. 2007. Lower branch coherent states in shear flows: Transition and control. *Phys. Rev. Lett.*, **98**, 204501.

- Wedin, H., and Kerswell, R. R. 2004. Exact coherent structures in pipe flow: travelling wave solutions. *J. Fluid Mech.*, **508**, 333–371.
- Wedin, H., Bottaro, A., and Nagata, M. 2009. Three-dimensional traveling waves in a square duct. *Phys. Rev. E*, **79**, 065305(R).
- Willis, A. P., and Kerswell, R. R. 2008. Coherent structures in localized and global pipe turbulence. *Phys. Rev. Lett.*, **100**, 124501.
- Willis, A. P., and Kerswell, R. R. 2009. Turbulent dynamics of pipe flow captured in a reduced model: puff relaminarization and localized ‘edge’ states. *J. Fluid Mech.*, **619**, 213–233.
- Wosnik, M., Castillo, L., and George, W. K. 2000. A theory for turbulent pipe and channel flows. *J. Fluid Mech.*, **421**, 115–145.
- Wu, X., and Moin, P. 2010. Transitional and turbulent boundary layer with heat transfer. *Phys. Fluids.*, **22**, 085105.
- Wyganski, I. J., and Champagne, F. H. 1973. On transition in a pipe. Part 1. The origin of puffs and slugs and the flow in a turbulent slug. *J. Fluid Mech.*, **59**, 281–335.
- Zhou, J., Adrian, R. J., S., Balachandar, and Kendall, T. M. 1999. Mechanisms for generating coherent packets of hairpin vortices in channel flow. *J. Fluid Mech.*, **387**, 353–396.